Toward genuinely high order embedded computations: a P1 Shifted Boundary Method with high order fluxes for Darcy problems

Léo Nouveau, Mario Ricchiuto, Guglielmo Scovazzi

Toward genuinely high order embedded computations: a P1 Shifted Boundary Method with high order fluxes for Darcy problems

L. Nouveau , M. Ricchiuto, G. Scovazzi

RESEARCH REPORT
N° 9204
September 2018
Project-Team CARDAMOM

ISSN 0249-6399 ISRN INRIA/RR--9204--FR+ENG

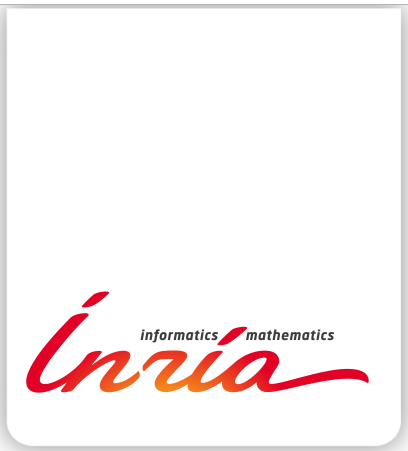

Toward genuinely high order embedded computations: a P1 Shifted Boundary Method with high order fluxes for Darcy problems

L. Nouveau *, M. Ricchiuto†, G. Scovazzi‡

Project-Team CARDAMOM

Research Report n° 9204 — September 2018 — 36 pages

Abstract: In this paper, we propose to extend the recent embedded boundary method known as "shifted boundary method" to the Darcy flow problems. The aim is to provide an improved formulation that would give, using linear approximation, at least second order accuracy on both flux and pressure variables, for any kind of boundary condition, considering embedded simulations. The strategy adopted here is to enrich the approximation of the pressure using Taylor expansions along the edges. The objective of this enrichment is to give a quadratic shape to the pressure. The resulted scheme provides high order accuracy on both variables for embedded simulations with an overall second order accuracy, that is bumped to third order for the pressure when only Dirichlet boundaries are embedded.

Key-words: embedded boundary; finite element method; approximate boundary; surrogate domain; stabilized methods; computational fluid dynamics; Darcy flow

* Department of Mechanical Engineering & Materials Science, Duke University, Durham, North Carolina 27708
† Team CARDAMOM, INRIA Bordeaux Sud-Ouest, 200 av. de la vieille tour, 33405 Talence Cedex, France
‡ Department of Civil & Environmental Engineering and Department of Mechanical Engineering & Materials Science, Duke University, Durham, North Carolina 27708

RESEARCH CENTRE
BORDEAUX – SUD-OUEST

200, Avenue de la Vieille Tour
33405 Talence Cedex

Vers des méthodes immergés generalisées: une approche Shifted Boundary P1 avec des flux d'ordre 2 pour les équations de Darcy

Résumé : Nous proposons une amélioration de la mode *shifted boundary* aux probls d'ulement de Darcy. L'objectif est de fournir une formulation qui permettrait, aide d'une approximation linre, au moins une prsion de second ordre sur les variables de flux et de pression, pour tout type de condition aux limites, en tenant compte une formulation immergé de conditions aux limites. La strate adoptci est d?enrichir l?approximation de la pression en utilisant un dloppement de Taylor le long des faces des éléments. Cet enrichissement, qui est basée sur les valeurs aux noeux des flux, permet d'obtenir une forme quadratique pression. Le sch rltant fournit une prsion vur les deux variables pour les simulations int avec une prsion globale du second ordre, qui est renvoyu troisi ordre pour la pression lorsque seules les limites de Dirichlet sont incorpor.

Mots-clés : méthodes immergés;conditions aux bords embedded; équations des ondes; équations de Darcy; milieux poreux; éléments finis; méthodes immergés

Contents

1 Introduction

Immersed and embedded boundary methods present several advantages with respect to conformal methods especially regarding mesh generation. If complex geometries are involved, generating the mesh can require considerable time and effort compared to the whole simulation process. In addition, when considering moving bodies or moving boundaries, conformal methods require complex and CPU time consuming remeshing procedures. Even though efficient approaches exist, based for example on Arbitrary Lagrangian Eulerian approximations an robust remeshing/projection techniques [20, 21, 22, 1, 2], the question is still very much open if these allow the same flexibility of immersed boundary approaches. Introduced by Peskin in 1972 [38], the Immersed Boundary Method (IBM) proposes to mesh the entire computational domain, independently of the geometry of the problem. Bodies or boundaries eventually present in the domain are then described implicitly on the mesh by some indicator such as e.g. a distance function. The method

was originally designed on cartesian grid, and its development has been an active field of research for some decades now. Two exhaustive reviews have been written by Mittal and Iaccarino in 2005 [33], and Sotiropoulos and Yang in 2014 [42]. The main idea behind IBM is to solve the model equations on the entire domain, and to impose the boundary conditions (BC) via a forcing term. The main drawback of this approach is the accuracy of boundary conditions which are most often only first order accurate. Some solutions have been proposed in the past to improve on this aspect, either by increasing the accuracy [14, 13, 25, 26], or by using mesh adaptation to balance its loss [37, 5, 15]. A similar objective is pursued by Embedded Boundary Methods. These approaches still use an *immersed* description of bodies and boundaries, however they solve the model equations only in the regions of interest. Within a finite element context, the most common approach is the cut-cell method [16, 7, 23, 43]. This technique usually combines a weak enforcement of the boundary conditions with a XFEM strategy, where an interface is reconstructed at the intersections between the boundary and the embedding grids. The drawback of these method is that they often lead to a complex implementation, and suffer from the so-called small-cut elements created during the intersection with the boundary, and characterized by extremely small sizes. These small-cut elements lead to a poor or ill- conditioning of the discrete problem.

In this work we follow the Shifted Boundary Method (SBM), firstly proposed by Main and Scovazzi for the Laplace and Stokes problem [27], then for the Navier-Stokes equations [28], and more recently applied to hyperbolic systems in [41]. The SBM has been written in a finite element context. The main idea is to impose the boundary conditions on a shifted boundary, called the surrogate boundary. The key idea of the method is to properly modify the condition imposed on this surrogate boundary so as to preserve the overall accuracy of the scheme. A Nitsche [36] technique provides a robust mechanism to weakly and consistently enforce the boundary conditions. The modified boundary value required on the surrogate boundary is defined using an extrapolation from within the computational domain of the value on the true boundary using a Taylor expansion. This strategy has been proven to be extremely robust and accurate for Dirichlet conditions. Some additional work is ongoing to improve the Neumann conditions, which require a corect estimation of higher derivatives to guarantee a sufficiently accurate extrapolation (at least second derivatives for second order). In [27] the authors have shown that the use of a reconstructed gradient may allow to overcome this issue.

An efficient strategy to enhance the accuracy of the method when considering Poisson or Darcy equations can be formulated when working with a mixed formulation. The main ideas have been put forward for fitted computations in [34, 30, 31, 32], based on earlier work by Caraeni [6]. The schemes proposed in these references to dicretize Poisson, diffusion, or advection diffusion operators are based on two main ideas. The first is to use what has been long known as hyperbolic relaxation: the elliptic or parabolic equation is recast as a first order system with a spatial differential operator admitting real eigenvalues and linearly independent eigenvectors. This allows to use standard techniques typical of hyperbolic discretizations to define stabilization operators. The second idea, exploited here, is to use the knowledge of solution derivatives as main unknowns of the mixed form to enhance the discrete polynomial representation of the solution. This allows to enhance the accuracy of the solution, and in particular to obtain a uniform second order of accuracy for the solution derivatives.

This paper proposes an application of the SBM approach to the Darcy equation in mixed form. This model equation fides many applications in civil, geotechnical and petroleum engineering. We will consider both continuous (CG) and discontinuous (DG) finite element approximations. For simplicity we focus on on P^1 elements. The DG approach is quite popular in the study of Darcy flows because it provides the advantage of dealing easily with discontinuous data, as e.g. discontinuous permeability. They have proven to be robust for both hyperbolic and elliptic

problems. The interested reader can refer to [39, 9, 3, 10, 17, 40, 11] and references therein for an overview. The drawback of the discontinuous representation is the increase in the number of degrees of freedom. A lot of promising work exit to improve on this. We can mention for exmaple the hybridizable DG method [8], the enriched Galerkin approach [24], or the multiscale DG approach [19, 44]. These methods are however generally still quite complex to implement. For this reason, when smooth solutions are involved, a stabilized continuous Galerkin method [29] still presents real interest. In this work we start from quite classical finite element approximations, namely the stabilized CG scheme of Masud *et. al.* [29] and the interior penalty DG scheme of [10, 3]. We propose a reformulation of these methods embedding the boundary conditions which are imposed on a surrogate boundary. Appropriate extrapolation operators are introduced to shift these conditions, in the spirit of the SB method. To handle all types of boundary conditions with a uniform second order of accuracy for all variables, we use a quadratic enrichment of the main variable, the pressure, similar to the one proposed in [34, 30, 31, 32].

The numerical results show that the SB formulation allows to retain second order of accuracy for the pressure and first order for the flux in embedded computations. However, as in [27], a loss of accuracy is observed when considering embedded Neumann boundary conditions. The enriched SBM approach, however, proves to be fully second order in both pressure and flux when embedding any combination of Neumann and Dirichlet conditions, and allows to obtain third order of accuracy for the pressure if only the Dirichlet conditions are embedded, event though only the nodal values of the pressure are solved for. To obtain these results, one needs to extrapolated to the proper order the boundary conditions. The importance of including in the variational formulation an additional consistency condition on the tangent flux when embedding the Dirichlet flux, as suggested in [30], is also shown. The final formulation allows to recover within machine accuracy exact quadratic solutions of the Darcy equation, on P^1 elements.

The the paper is organized as follows: after a brief recall of the problem of interest in Section 2, general notions for CG and DG formulations are given Section 3, and definitions and notations regarding the shifted boundary method are given Section 4. Section 5 presents the original stabilized finite element scheme for both conformal and embedded configurations. Section 6 is devoted to the pressure enrichment and the construction of the improved schemes. Finally, the method is validated and tested over several test cases in Section 7.

2 Problem statement: Darcy flow

The Darcy flow equations provide a homogenized macroscopic transport model through porous media. The problem is ruled by the following set of equations:

$$\begin{cases} \boldsymbol{\Lambda}^{-1}\boldsymbol{\beta} + \boldsymbol{\nabla} p = 0 & \text{in } \Omega \\ \boldsymbol{\nabla}\cdot\boldsymbol{\beta} = \phi & \text{in } \Omega \\ p = p_D & \text{on } \Gamma_D \\ \boldsymbol{\beta}\cdot\boldsymbol{n} = h_N & \text{on } \Gamma_N \end{cases} \tag{1}$$

where $\boldsymbol{\beta}$ denotes the flux, p the pressure, $\boldsymbol{\Lambda}$ the permeability matrix and ϕ a source term. Note that the permeability is in general spatially dependent, *i.e.* $\boldsymbol{\Lambda} = \boldsymbol{\Lambda}(\boldsymbol{x})$,and may even be discontinuous The boundary of the computational domain Ω is noted by $\partial\Omega$, and partitioned into Γ_D and Γ_N, on which Dirichlet and Neumann boundary conditions (BC) are imposed. Obviously we have $\partial\Omega = \Gamma_N \cup \Gamma_D$, $\Gamma_N \cap \Gamma_D = \emptyset$.

3 General notations for Galerkin methods

Let $\mathcal{T}_h$ denote a tesselation of the domain Ω, composed of non-overlapping regular elements K, with $\mathcal{T}_h = \cup K$. For a given element K, we denote by by $|K|$ its area, by ∂K its boundary, by γ_K a generic face/edge, and by h_K its reference length. We denote the reference mesh size by $h = \max_{K\in\mathcal{T}_h} h_K$. The set of internal edges is denoted by $\mathcal{E}_i$,and for an interior edge γ_K, K^+ and K^- are the elements on each side of it. For a given face/edge $\gamma_K \in \mathcal{T}_h$ of size $|\gamma_K|$, the characteristic length in a direction perpendicular to it is denoted by $h^\perp$, and computed as :

$$h^\perp = \begin{cases} \dfrac{|K^+| + |K^-|}{2|\gamma_K|} & \text{if } \gamma_K \cap \partial\Omega = \emptyset \\ \dfrac{|K|}{2|\gamma_K|} & \text{if } \gamma_K \cap \partial\Omega \neq \emptyset \end{cases} \tag{2}$$

The mesh is assumed to verify classical regularity assumptions. In particular it is assumed that there exist bounded constants $\zeta_1, \zeta_2 \in \mathbb{R}^+$ such that:

$$\zeta_1 h \leq h^\perp \leq \zeta_2 h \tag{3}$$

Let us now introduce some common spaces that will be used to build DG and CG schemes. The discontinuous Galerkin spaces are defined as:

$$\begin{aligned} S_d^l(\Omega) &= \left\{ p \in L^2(\Omega) : p|_K \in \mathbb{P}^l(K), \forall K \in \mathcal{T}_h \right\} \\ \boldsymbol{V}_d^k(\Omega) &= \left\{ \boldsymbol{\beta} \in \left(L^2(\Omega)\right)^d : \boldsymbol{\beta}|_K \in \left(\mathbb{P}^k(K)\right)^d, \forall K \in \mathcal{T}_h \right\} \end{aligned} \tag{4}$$

where $\mathbb{P}^n(K)$ is the space of polynomial function of order at most n on K. From those spaces, and denoting by $C(\Omega)$ the set of continuous functions on Ω, the continuous Galerkin spaces are defined as:

$$\begin{aligned} S_c^l(\Omega) &= S_d^l(\Omega) \cap C(\Omega) \\ \boldsymbol{V}_c^k(\Omega) &= \boldsymbol{V}_d^k(\Omega) \cap (C(\Omega))^d \end{aligned} \tag{5}$$

We also introduce the tensor product spaces $\boldsymbol{M}_d(\Omega) = \boldsymbol{V}_d^k(\Omega) \times S_d^l(\Omega)$ and $\boldsymbol{M}_c(\Omega) = \boldsymbol{V}_c^k(\Omega) \times S_c^l(\Omega)$. The $L^2(K)$ inner products over an element and its boundary are defined as:

$$\begin{aligned} (v,w)_K &= \int_K vw \qquad \text{and} \qquad (\boldsymbol{v},\boldsymbol{w})_K = \int_K \boldsymbol{v}\cdot\boldsymbol{w} \\ < u, v >_{\partial K} &= \int_{\partial K} uv \qquad \text{and} \qquad < \boldsymbol{u}, \boldsymbol{v} >_{\partial K} = \int_K \boldsymbol{v}\cdot\boldsymbol{w} \end{aligned} . \tag{6}$$

Next, we introduce the average and jump operators $\{.\}$ and $[\![.]\!]$ for discontinuous scalar and vector fields as follows:

$$\begin{aligned} \{p\} &= \frac{1}{2}(p^+ + p^-) & [\![p]\!] &= p^+\boldsymbol{n}^+ + p^-\boldsymbol{n}^- \\ \{\boldsymbol{\beta}\} &= \frac{1}{2}(\boldsymbol{\beta}^+ + \boldsymbol{\beta}^-) & [\![\boldsymbol{\beta}]\!] &= \boldsymbol{\beta}^+\cdot\boldsymbol{n}^+ + \boldsymbol{\beta}^-\cdot\boldsymbol{n}^- \end{aligned} \tag{7}$$

where the $+$ and $-$ signs indicate the two sides of and edge/face. By a reordering/bookkeeping, the following useful equality can be proved:

$$\sum_K < w, \boldsymbol{v}\cdot\boldsymbol{n} >_{\partial K} = < \{w\}, [\![\boldsymbol{v}]\!] >_{\mathcal{E}_i} + < [\![w]\!], \{\boldsymbol{v}\} >_{\mathcal{E}_i} + < w, \boldsymbol{v}\cdot\boldsymbol{n} >_{\partial\Omega} \tag{8}$$

4 General notations for embedded approach, true and surrogate domains

Let us consider now an embedded discretization in which the computational grid does not conform to the boundary (see figure 1). The notion of *surrogate boundary* $\tilde{\Gamma}$ needs to be introduced. It is composed of the faces/edges of the mesh that are the closest to the true boundary Γ. $\tilde{\Gamma}$ can be constructed, for example, by computing the intersections of the grid and the true boundary Γ and using closest-point projection algorithms to detect the closet face/edge of $\tilde{\Gamma}$ to Γ. Other choices are of course possible, such as level-set functions for instance, as long as the overall topology of Γ and $\tilde{\Gamma}$ are close to each other, that is if Γ has a certain number of holes, the same number of holes needs to be also present in $\tilde{\Gamma}$. The surrogate boundary $\tilde{\Gamma}$ encloses the *surrogate domain* $\tilde{\Omega}$. In particular, $\tilde{n}$ indicates the unit outward normal of $\tilde{\Gamma}$, to be distinguished from the outward normal $\boldsymbol{n}$ of Γ. The mapping from the surrogate to true interface is then defined as:

$$\begin{aligned} \boldsymbol{M} :\tilde{\Gamma} &\rightarrow \Gamma, \\ \tilde{\boldsymbol{x}} &\mapsto \boldsymbol{x} \end{aligned} \tag{9}$$

In particular, the map $\boldsymbol{M}$ can be characterized through a distance vector function:

$$\boldsymbol{d}_M(\tilde{\boldsymbol{x}}) = \boldsymbol{x} - \tilde{\boldsymbol{x}} = [\boldsymbol{M} - \boldsymbol{I}](\tilde{\boldsymbol{x}}) \tag{10}$$

In the following, we will simply define the distance vector function as $\boldsymbol{d}$, which can be linked to the normal of the true boundary as:

$$\boldsymbol{n} = \frac{\boldsymbol{d}}{||\boldsymbol{d}||} \tag{11}$$

We recall here a property that has been of major importance in the original design of the SB method [27]:

Assumption 1. *The vector distance $\boldsymbol{d}$ is defined as $\boldsymbol{d} = ||\boldsymbol{d}||\boldsymbol{n}$, where the normal $\boldsymbol{n}$ to the true boundary and the normal $\tilde{\boldsymbol{n}}$ to the surrogate boundary satisfy:*

$$\boldsymbol{n} \cdot \tilde{\boldsymbol{n}} \geq 0 \tag{12}$$

Through the map $\boldsymbol{M}$, it is possible to define the extension $\overline{\psi}$ on $\tilde{\Gamma}$ of a function ψ originally defined on Γ, as:

$$\overline{\psi}(\tilde{\boldsymbol{x}}) \equiv \psi(\boldsymbol{M}(\tilde{\boldsymbol{x}})) \tag{13}$$

For instance, the unit normal $\boldsymbol{n}$ and tangential vectors $\boldsymbol{\tau}_i$ ($1 < i < n_d$) of the true boundary Γ can be extended to the boundary $\tilde{\Gamma}$ as follows:

$$\begin{aligned} \overline{\boldsymbol{n}}(\tilde{\boldsymbol{x}}) &\equiv \boldsymbol{n}(\boldsymbol{M}(\tilde{\boldsymbol{x}})), \\ \overline{\boldsymbol{\tau}}_i(\tilde{\boldsymbol{x}}) &\equiv \boldsymbol{\tau}_i(\boldsymbol{M}(\tilde{\boldsymbol{x}})) \end{aligned} \tag{14}$$

For sake of simplification in the notation, we will omit the bar in the expressions when considering normal and tangents and thus write $\boldsymbol{n}(\tilde{\boldsymbol{x}})$ and $\boldsymbol{\tau}_i(\tilde{\boldsymbol{x}})$. We can also introduce the derivatives in the directions $\boldsymbol{n}$ and $\boldsymbol{\tau}_i$ of a function ψ at a point $\tilde{\boldsymbol{x}} \in \tilde{\Gamma}$:

$$\begin{aligned} \psi_{,\boldsymbol{n}}(\tilde{\boldsymbol{x}}) &= \boldsymbol{\nabla}\psi(\tilde{\boldsymbol{x}}) \cdot \boldsymbol{n}(\tilde{\boldsymbol{x}}) \\ \psi_{,\boldsymbol{\tau_i}}(\tilde{\boldsymbol{x}}) &= \boldsymbol{\nabla}\psi(\tilde{\boldsymbol{x}}) \cdot \boldsymbol{\tau}_i(\tilde{\boldsymbol{x}}) \end{aligned} \tag{15}$$

These constructions are particularly useful if we consider the solution u to a partial differential equation and, for example, we desire to build an extension of the Dirichlet boundary condition

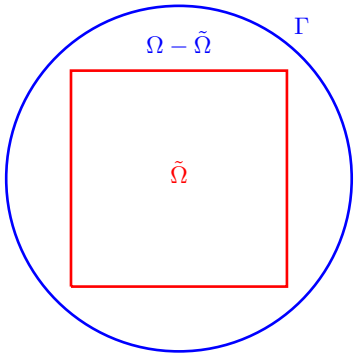

(a) Surrogate domain $\tilde{\Omega}$ and true one Ω

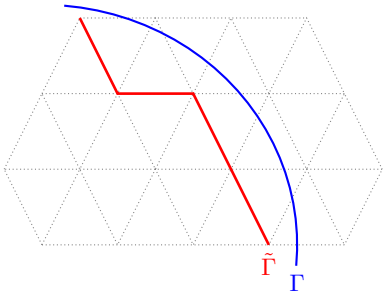

(b) Surrogate and true boundary $\tilde{\Gamma}$ and Γ

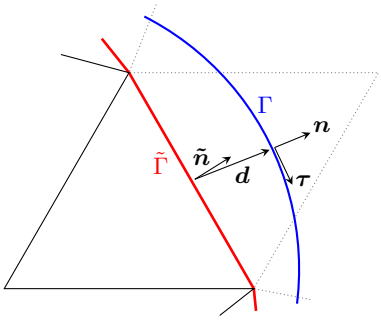

(c) Distance vector $\boldsymbol{d}$, tangent vector τ and normal vector $\boldsymbol{n}$ of the true boundary. Normal vector $\tilde{\boldsymbol{n}}$ of the surrogate boundary

Figure 1: Surrogate and true domain/boundary, notations.

u_D from the true boundary Γ_D to a surrogate boundary $\tilde{\Gamma}_D$. In particular, the following Taylor expansion centered at $\tilde{\boldsymbol{x}} \in \tilde{\Gamma}_D$ holds for $\boldsymbol{x} = \boldsymbol{M}(\tilde{\boldsymbol{x}}) = \tilde{\boldsymbol{x}} + \boldsymbol{d}(\tilde{\boldsymbol{x}}) \in \Gamma_D$:

$$\begin{aligned} u_D(\boldsymbol{x}) &= u_D(\tilde{\boldsymbol{x}} + \boldsymbol{d}(\tilde{\boldsymbol{x}})) \\ &= u_D(\tilde{\boldsymbol{x}}) + \boldsymbol{\nabla} u(\tilde{\boldsymbol{x}}) \cdot \boldsymbol{d}(\tilde{\boldsymbol{x}}) + \frac{1}{2} \boldsymbol{d}^T(\tilde{\boldsymbol{x}}) \boldsymbol{\mathcal{H}}(u) \boldsymbol{d}(\tilde{\boldsymbol{x}}) + \mathcal{O}(||\boldsymbol{d}(\tilde{\boldsymbol{x}})||^3) \end{aligned} \tag{16}$$

where $\boldsymbol{\mathcal{H}}(u)$ denotes the Hessian of u. This last expression can be used to develop a new strategy for the imposition of Dirichlet boundary conditions in the context of embedded methods. According to the wanted accuracy, more or less terms are added to the Taylor expansion.

5 Continuous and discontinuous finite element scheme for Darcy flow

5.1 Variational formulation: conformal case

We briefly recall here the construction of discontinuous Galerkin scheme and refer to [9, 3, 10] and references therein for more details. The starting point is to multiply each equation of the

Darcy problem (1) by the test functions $(\boldsymbol{w}, q) \in \boldsymbol{M}_d(\Omega)$ and to integrate over a generic triangle:

$$\begin{aligned}(\boldsymbol{w}, \boldsymbol{\Lambda^{-1}\beta})_K + (\boldsymbol{w}, \boldsymbol{\nabla} p)_K = (\boldsymbol{w}, \boldsymbol{\Lambda^{-1}\beta})_K - (\boldsymbol{\nabla}\cdot\boldsymbol{w}, p)_K + <\boldsymbol{w}\cdot\boldsymbol{n}, p>_{\partial K} = 0 \\ (q, \boldsymbol{\nabla}\cdot\boldsymbol{\beta})_K = -(\boldsymbol{\nabla} q, \boldsymbol{\beta})_K + <q, \boldsymbol{\beta}\cdot\boldsymbol{n}>_{\partial K} = (q, \phi)_K\end{aligned} \tag{17}$$

The boundary traces are then replaced by the *numerical fluxes* $\hat{p}$, $\hat{\boldsymbol{\beta}}$ and an integration by part is performed again on the second equation before summing on all the elements of the mesh:

$$\begin{aligned}(\boldsymbol{w}, \boldsymbol{\Lambda^{-1}\beta})_\Omega - (\boldsymbol{\nabla}\cdot\boldsymbol{w}, p)_\Omega + \sum_K <\boldsymbol{w}\cdot\boldsymbol{n}, \hat{p}>_{\partial K} = 0 \\ (q, \boldsymbol{\nabla}\cdot\boldsymbol{\beta})_\Omega + \sum_K <q, (\hat{\boldsymbol{\beta}} - \boldsymbol{\beta})\cdot\boldsymbol{n}>_{\partial K} = (q, \phi)_\Omega\end{aligned} \tag{18}$$

The numerical fluxes act as a communication of the discontinuous polynomial approximations of the solution between neighboring elements. Using the definition of average and jump operators along with equality (8), the set of equations (18) become:

$$\begin{aligned}(\boldsymbol{w}, \boldsymbol{\Lambda^{-1}\beta})_\Omega - (\boldsymbol{\nabla}\cdot\boldsymbol{w}, p)_\Omega + <[\![\boldsymbol{w}]\!], \{\hat{p}\}>_{\mathcal{E}_i} + <\{\boldsymbol{w}\}, [\![\hat{p}]\!]>_{\mathcal{E}_i} + <\boldsymbol{w}\cdot\boldsymbol{n}, \hat{p}>_{\partial\Omega} = 0 \\ (q, \boldsymbol{\nabla}\cdot\boldsymbol{\beta})_\Omega + <[\![q]\!], \{\hat{\boldsymbol{\beta}} - \boldsymbol{\beta}\}>_{\mathcal{E}_i} + <\{q\}, [\![\hat{\boldsymbol{\beta}} - \boldsymbol{\beta}]\!]>_{\mathcal{E}_i} + <q, (\hat{\boldsymbol{\beta}} - \boldsymbol{\beta})\cdot\boldsymbol{n}>_{\partial\Omega} = (q, \phi)_\Omega\end{aligned} \tag{19}$$

The definition of the numerical fluxes differentiates the different DG formulations. In this work, we follow the approach of the *Interior Penalty* (IP) method [10, 3], and the numerical fluxes are defined as:

$$\begin{cases}\hat{p} = \{p\} + \alpha_p [\![\boldsymbol{\beta}]\!], & \hat{\boldsymbol{\beta}} = \{\boldsymbol{\beta}\} + \alpha_\beta [\![p]\!], & \text{on } \mathcal{E}_i \\ \hat{p} = p_D, & \hat{\boldsymbol{\beta}} = \boldsymbol{\beta} + \alpha_\beta (p - p_D)\boldsymbol{n} & \text{on } \Gamma_D \\ \hat{p} = p, & \hat{\boldsymbol{\beta}}\cdot\boldsymbol{n} = h_N & \text{on } \Gamma_N\end{cases} \tag{20}$$

where the penalty coefficients α_p, α_β are defined as $\alpha_\beta = \tilde{\alpha}_\beta/(h^\perp)||\boldsymbol{\Lambda}||$ and $\alpha_p = \tilde{\alpha}_p h^\perp/||\boldsymbol{\Lambda}||$ with $\tilde{\alpha}$ real positive constants. As proposed in [18], a stabilizing term similar to the one employed to the continuous formulation [29] can be added and the final formulation writes:

$$\begin{aligned}B_d(\boldsymbol{w}, q; \boldsymbol{\beta}, p) &= B_d^{Gal}(\boldsymbol{w}, q; \boldsymbol{\beta}, p) + B^{Stab}(\boldsymbol{w}, q; \boldsymbol{\beta}, p) = L_d^{Gal}(\boldsymbol{w}, q) + L^{Stab}(\boldsymbol{w}, q) \\ B_d^{Gal}(\boldsymbol{w}, q; \boldsymbol{\beta}, p) &= (\boldsymbol{w}, \boldsymbol{\Lambda^{-1}\beta})_\Omega - (\boldsymbol{\nabla}\cdot\boldsymbol{w}, p)_\Omega + (q, \boldsymbol{\nabla}\cdot\boldsymbol{\beta})_\Omega + <[\![\boldsymbol{w}]\!], \{p\}>_{\mathcal{E}_i} - <\{q\}, [\![\boldsymbol{\beta}]\!]>_{\mathcal{E}_i} + <[\![q]\!], \alpha_\beta [\![p]\!]>_{\mathcal{E}_i} \\ &\quad + <[\![\boldsymbol{w}]\!], \alpha_p [\![\boldsymbol{\beta}]\!]>_{\mathcal{E}_i} + <\boldsymbol{w}\cdot\boldsymbol{n}, p>_{\Gamma_N} - <q, \boldsymbol{\beta}\cdot\boldsymbol{n}>_{\Gamma_N} + <q, \alpha_\beta p>_{\Gamma_D} \\ B^{Stab}(\boldsymbol{w}, q; \boldsymbol{\beta}, p) &= \frac{1}{2}\left(-\boldsymbol{\Lambda^{-1}w} + \boldsymbol{\nabla} q, \boldsymbol{\beta} + \boldsymbol{\Lambda\nabla} p\right)_\Omega + \frac{\zeta}{2}\left(\boldsymbol{\nabla}\cdot\boldsymbol{w}, ||\boldsymbol{\Lambda}|| h^2 \boldsymbol{\nabla}\cdot\boldsymbol{\beta}\right)_\Omega \\ L_d^{Gal}(\boldsymbol{w}, q) &= (q, \phi)_\Omega - <\boldsymbol{w}\cdot\boldsymbol{n}, p_D>_{\Gamma_D} + <q, \alpha_\beta p_D>_{\Gamma_D} - <q, h_N>_{\Gamma_N} \\ L^{Stab}(\boldsymbol{w}, q) &= \frac{\zeta}{2}(\boldsymbol{\nabla}\cdot\boldsymbol{w}, ||\boldsymbol{\Lambda}|| h^2 \phi)_\Omega\end{aligned} \tag{21}$$

with ζ a constant $\zeta = \mathcal{O}(1)$. From this discontinuous scheme (21), the continuous stabilized formulation can be obtained by cancelling every internal edge term containing a jump, and replacing averages of the unknowns and of the test functions by their unique continuous values.

In [18, 29], stability and convergence has been proven defining the following stability norm:

$$|||(\boldsymbol{\beta}, p)|||^2 = ||\boldsymbol{\Lambda^{1/2}\beta}||_\Omega + ||\boldsymbol{\Lambda^{1/2}\nabla} p||_\Omega + ||(h^\perp)^{-1/2}||\boldsymbol{\Lambda}||^{1/2}[\![p]\!]||_{\mathcal{E}_i} + ||(h^\perp)^{-1/2}||\boldsymbol{\Lambda}||^{1/2} p||_{\Gamma_D} \tag{22}$$

with the following error estimate:

$$|||\boldsymbol{\beta}_e - \boldsymbol{\beta}, p_e - p|||^2 \leq C_1 h^{k+1}|\boldsymbol{\beta}|_{k+1} + C_2 h^l |p|_{l+1} \tag{23}$$

where C_1 and C_2 are two constants. Such a scheme is thus converging with order $r = \min(k+1, l)$ for the flux and $r+1$ for the pressure. Thus for linear approximations, as will be illustrated later in section 7, the pressure is second order accurate and the flux first order.

Remark 1. *The definition of the numerical fluxes (20) can be related to the variational multiscale approach proposed by Badia and Codina [4].*

5.2 Variational formulation: embedded case

We now propose to extend the scheme (21) to an embedded formulation, using the SB method [27, 28]. Looking at equations (19), the integrations over internal edges are not impacting by the integration on the surrogate domain. However, the boundary integral on the surrogate domain $\partial\tilde{\Omega}$ now involve the surrogate normal $\tilde{\boldsymbol{n}}$. Thus, equations (19) are written as:

$$(\boldsymbol{w}, \boldsymbol{\Lambda}^{-1}\boldsymbol{\beta})_{\tilde{\Omega}} - (\boldsymbol{\nabla}\cdot\boldsymbol{w}, p)_{\tilde{\Omega}} + < [\![\boldsymbol{w}]\!], \{\hat{p}\} >_{\mathcal{E}_i} + < \{\boldsymbol{w}\}, [\![\hat{p}]\!] >_{\mathcal{E}_i} + < \boldsymbol{w}\cdot\tilde{\boldsymbol{n}}, \hat{p} >_{\partial\tilde{\Omega}} = 0 \tag{24}$$

$$(q, \boldsymbol{\nabla}\cdot\boldsymbol{\beta})_{\tilde{\Omega}} + < [\![q]\!], \{\hat{\boldsymbol{\beta}} - \boldsymbol{\beta}\} >_{\mathcal{E}_i} + < \{q\}, [\![\hat{\boldsymbol{\beta}} - \boldsymbol{\beta}]\!] >_{\mathcal{E}_i} + < q, (\hat{\boldsymbol{\beta}} - \boldsymbol{\beta})\cdot\tilde{\boldsymbol{n}} >_{\partial\tilde{\Omega}} = (q, \phi)_{\tilde{\Omega}} \tag{25}$$

The definition of the numerical fluxes needs to be modified accordingly on the boundaries. The main difference arises for Neumann boundary conditions. Indeed, as the value to impose on the flux is in the normal direction of the true boundary, the first step is to decompose the surrogate normal $\tilde{\boldsymbol{n}}$ onto the normal $\boldsymbol{n}$ and tangents $\boldsymbol{\tau}_i$ of the true boundary, and the term in equation (25) writes for the integral on Neumann boudaries:

$$< q, (\hat{\boldsymbol{\beta}} - \boldsymbol{\beta})\cdot\tilde{\boldsymbol{n}} >_{\tilde{\Gamma}_N} = < q(\boldsymbol{n}\cdot\tilde{\boldsymbol{n}}), (\hat{\boldsymbol{\beta}} - \boldsymbol{\beta})\cdot\boldsymbol{n} >_{\tilde{\Gamma}_N} + < q(\boldsymbol{\tau}_i\cdot\tilde{\boldsymbol{n}}), (\hat{\boldsymbol{\beta}} - \boldsymbol{\beta})\cdot\boldsymbol{\tau}_i >_{\tilde{\Gamma}_N} \tag{26}$$

We impose the following condition on the tangential flux:

$$\hat{\boldsymbol{\beta}}\cdot\boldsymbol{\tau}_i = \boldsymbol{\beta}\cdot\boldsymbol{\tau}_i, \text{ on } \tilde{\Gamma}_N \tag{27}$$

Then, omitting the stabilization terms, the scheme (21) reads:

$$(\boldsymbol{w}, \boldsymbol{\Lambda}^{-1}\boldsymbol{\beta})_{\tilde{\Omega}} - (\boldsymbol{\nabla}\cdot\boldsymbol{w}, p)_{\tilde{\Omega}} + (q, \boldsymbol{\nabla}\cdot\boldsymbol{\beta})_{\tilde{\Omega}} + < [\![\boldsymbol{w}]\!], \{p\} >_{\mathcal{E}_i} - < \{q\}, [\![\boldsymbol{\beta}]\!] >_{\mathcal{E}_i} + < [\![q]\!], \alpha_\beta [\![p]\!] >_{\mathcal{E}_i} + < [\![\boldsymbol{w}]\!], \alpha_p [\![\boldsymbol{\beta}]\!] >_{\mathcal{E}_i}$$
$$+ < \boldsymbol{w}\cdot\tilde{\boldsymbol{n}}, p >_{\tilde{\Gamma}_N} - < q(\boldsymbol{n}\cdot\tilde{\boldsymbol{n}}), \boldsymbol{\beta}\cdot\boldsymbol{n} - h_N) >_{\tilde{\Gamma}_N} + < \boldsymbol{w}\cdot\tilde{\boldsymbol{n}}, p_D >_{\tilde{\Gamma}_D} + < q, \alpha_\beta(p - p_D) >_{\tilde{\Gamma}_D} = 0 \tag{28}$$

However, p_D and h_N are the values that would be imposed for the pressure and normal flux on the true boundaries Γ_D and Γ_N, and the integrations are performed on the surrogate ones $\tilde{\Gamma}_D$ and $\tilde{\Gamma}_N$. Thus, the boundary conditions need to be modified accordingly so as to preserve the accuracy of the schemes.

5.2.1 Shifted Dirichlet boundary conditions

To preserve the accuracy when integrating on the surrogate boundaries, an accurate approximation of the true condition needs to be defined. We propose to follow the methodology developed in [27], with the theory and notations proposed section 4. The Taylor expansion (16) is employed to extend the known function p_D from the true boundaries Γ_D onto the surrogate ones $\tilde{\Gamma}_D$. For Dirichlet boundary conditions, it reads:

$$\overline{p}_D = p_D(\tilde{\boldsymbol{x}}) + \boldsymbol{\nabla}p\cdot\boldsymbol{d} + \mathcal{O}(||\boldsymbol{d}||^2) \tag{29}$$

Thus on the Dirichlet boundary integrals, p_D needs to be substituted by its extended value $\bar{p}_D - \boldsymbol{\nabla}p\cdot\boldsymbol{d}$.

5.2.2 Shifted Neumann boundary condition

Similarly to Dirichlet boundary condition, the value h_N needs to be extended from the true boundary Γ_N to the surrogate one $\tilde{\Gamma}_N$. Thus, the Taylor expansion is employed as:

$$\bar{h}_N = \boldsymbol{\beta}(\tilde{\boldsymbol{x}}) \cdot \boldsymbol{n} + [(\boldsymbol{\nabla}\boldsymbol{\beta})\boldsymbol{d}] \cdot \boldsymbol{n} + \mathcal{O}(||\boldsymbol{d}||^2) \tag{30}$$

And thus, for the integral involved on Neumann boundaries, the normal flux needs to be evaluated as $\bar{h}_N - [(\boldsymbol{\nabla}\boldsymbol{\beta})\boldsymbol{d}] \cdot \boldsymbol{n}$ instead of h_N.

5.2.3 Embedded finite element scheme

Using now the corrected values of the boundary conditions (29,30), the final discontinuous weak formulation of the problem for the shifted boundary method reads:

$$\begin{aligned}
B_d(\boldsymbol{w},q;\boldsymbol{\beta},p) &= B_d^{Gal}(\boldsymbol{w},q;\boldsymbol{\beta},p) + B^{Stab}(\boldsymbol{w},q;\boldsymbol{\beta},p) = L_d^{Gal}(\boldsymbol{w},q) + L^{Stab}(\boldsymbol{w},q)\\
B_d^{Gal}(\boldsymbol{w},q;\boldsymbol{\beta},p) &= (\boldsymbol{w},\boldsymbol{\Lambda}^{-1}\boldsymbol{\beta})_{\tilde{\Omega}} - (\boldsymbol{\nabla}\cdot\boldsymbol{w},p)_{\tilde{\Omega}} + (q,\boldsymbol{\nabla}\cdot\boldsymbol{\beta})_{\tilde{\Omega}} + <[\![\boldsymbol{w}]\!],\{p\}>_{\mathcal{E}_i} - <\{q\},[\![\boldsymbol{\beta}]\!]>_{\mathcal{E}_i} + <[\![q]\!],\alpha_\beta[\![p]\!]>_{\mathcal{E}_i}\\
&\quad + <[\![\boldsymbol{w}]\!],\alpha_p[\![\boldsymbol{\beta}]\!]>_{\mathcal{E}_i} + <\boldsymbol{w}\cdot\tilde{\boldsymbol{n}},p>_{\tilde{\Gamma}_N} - <q(\boldsymbol{n}\cdot\tilde{\boldsymbol{n}}),(\boldsymbol{\beta}+[\boldsymbol{\nabla}\boldsymbol{\beta}]\boldsymbol{d})\cdot\boldsymbol{n}>_{\tilde{\Gamma}_N} - <\boldsymbol{w}\cdot\tilde{\boldsymbol{n}},\boldsymbol{\nabla}p\cdot\boldsymbol{d}>_{\tilde{\Gamma}_D}\\
&\quad + <q+\boldsymbol{\nabla}q\cdot\boldsymbol{d},\alpha_\beta(p+\boldsymbol{\nabla}p\cdot\boldsymbol{d})>_{\tilde{\Gamma}_D}\\
L_d^{Gal}(\boldsymbol{w},q) &= (q,\phi)_{\tilde{\Omega}} - <\boldsymbol{w}\cdot\tilde{\boldsymbol{n}},\bar{p}_D>_{\tilde{\Gamma}_D} + <q+\boldsymbol{\nabla}q\cdot\boldsymbol{d},\alpha\bar{p}_D>_{\tilde{\Gamma}_D} - <q(\boldsymbol{n}\cdot\tilde{\boldsymbol{n}}),\bar{h}_N>_{\tilde{\Gamma}_N}
\end{aligned} \tag{31}$$

Once again, the continuous stabilized finite element scheme is obtained from (31) by canceling all the internal edge integrals containing jumps. The resulting variational formulation reads:

$$\begin{aligned}
B_c(\boldsymbol{w},q;\boldsymbol{\beta},p) &= B_c^{Gal}(\boldsymbol{w},q;\boldsymbol{\beta},p) + B^{Stab}(\boldsymbol{w},q;\boldsymbol{\beta},q) = L_c^{Gal}(\boldsymbol{w},q) + L^{Stab}(\boldsymbol{w},q)\\
B_c^{Gal}(\boldsymbol{w},q;\boldsymbol{\beta},p) &= (\boldsymbol{w},\boldsymbol{\Lambda}^{-1}\boldsymbol{\beta})_{\tilde{\Omega}} - (\boldsymbol{\nabla}\cdot\boldsymbol{w},p)_{\tilde{\Omega}} + (q,\boldsymbol{\nabla}\cdot\boldsymbol{\beta})_{\tilde{\Omega}} + <\boldsymbol{w}\cdot\tilde{\boldsymbol{n}},p>_{\tilde{\Gamma}_N} - <q(\boldsymbol{n}\cdot\tilde{\boldsymbol{n}}),(\boldsymbol{\beta}+[\boldsymbol{\nabla}\boldsymbol{\beta}]\boldsymbol{d})\cdot\boldsymbol{n}>_{\tilde{\Gamma}_N}\\
&\quad + <\boldsymbol{w}\cdot\tilde{\boldsymbol{n}},\boldsymbol{\nabla}p\cdot\boldsymbol{d}>_{\tilde{\Gamma}_D} + <q+\boldsymbol{\nabla}q\cdot\boldsymbol{d},\alpha_\beta(p+\boldsymbol{\nabla}p\cdot\boldsymbol{d})>_{\tilde{\Gamma}_D}\\
L_c^{Gal}(\boldsymbol{w},q) &= (q,\phi)_{\tilde{\Omega}} - <\boldsymbol{w}\cdot\tilde{\boldsymbol{n}},\bar{p}_D>_{\tilde{\Gamma}_D} + <q+\boldsymbol{\nabla}q\cdot\boldsymbol{d},\alpha_\beta\bar{p}_D>_{\tilde{\Gamma}_D} - <q(\boldsymbol{n}\cdot\tilde{\boldsymbol{n}}),\bar{h}_N>_{\tilde{\Gamma}_N}
\end{aligned} \tag{32}$$

From this continuous Galerkin formulation (32), the Euler-Lagrange equations can be obtained by performing integration by parts. The resulting expression is:

$$\begin{aligned}
&(\boldsymbol{w},(\boldsymbol{\Lambda}^{-1}\boldsymbol{\beta}+\boldsymbol{\nabla}p))_{\tilde{\Omega}} + (q,(\boldsymbol{\nabla}\cdot\boldsymbol{\beta}-\phi))_{\tilde{\Omega}}\\
&- <\boldsymbol{w}\cdot\tilde{\boldsymbol{n}}+\alpha_\beta(q+\boldsymbol{\nabla}\cdot\boldsymbol{d}),p+\boldsymbol{\nabla}p\cdot\boldsymbol{d}-\bar{p}_D>_{\tilde{\Gamma}_D}\\
&- <q(\boldsymbol{n}\cdot\tilde{\boldsymbol{n}}),(\boldsymbol{\beta}+(\boldsymbol{\nabla}\boldsymbol{\beta})\boldsymbol{d})\cdot\boldsymbol{n}-\bar{h}_N>_{\tilde{\Gamma}_N} = 0
\end{aligned} \tag{33}$$

The Euler-Legrange equations tell us the consistency conditions being enforced by the scheme. We can see that the SB method enforces the partial differential equation on the interior surrogate domain $\tilde{\Omega}$. Regarding the Dirichlet boundary conditions, the term corresponds to the imposition of the extended value of the pressure condition using the Taylor expansion. This term, although coming from the DG scheme can be seen in the continuous case as a Nitsche weak imposition of the boundary condition [36]. Identically, the last term corresponds to the Neumann imposition of the boundary condition, with the second order correction of the boundary value on the surrogate domain.

As will be illustrated in the last section of this paper 7, this formulation (31) provides in numerical applications a first order flux, and a second order pressure for Dirichlet boundary conditions. The accuracy of the latter falls to first order when embedded Neumann conditions are considered. Our aim is to improve the formulation so that second order of accuracy may be obtained possibly for both pressure and flux regardless of which boundary condition is embedded. The next section is devoted to this enhancement.

6 Pressure enrichment and high order flux finite element scheme

We propose here to modify schemes (21), and (31) with the aim to obtain at second order accuracy on both pressure and for any kind of embedded BC. In [30], based on the earlier work of [6, 34], Mazaheri and Nishikawa propose a genuine way to improve accuracy of advection-diffusion problems by appropriately exploiting the mixed form of the problem. In particular, by exploiting the relations between the flux and the pressure gradients in the Darcy equation, we can construct a quadratic discrete approximation of the pressure. This *pressure enrichment* is discussed in the following section.

6.1 Enriched pressure approximation

Our aim is to to define a quadratic pressure polynomial in each element. One way to achieve this is to add additional degrees of freedom associated to the pressure values at edge midpoints, as illustrated (for simplicity in two dimensions) on Figure 2. These additional degrees of freedom become unknowns of the problem and thus the size of the system to solve increases. The resulting **red**P^4 approximation u_h of a variable u reads:

$$u_h(\boldsymbol{x}) = \sum_{iP^1} u_i \varphi_i^{P^2}(\boldsymbol{x}) + \sum_{jP^2} u_j \varphi_j^{P^2}(\boldsymbol{x}) \tag{34}$$

where the u_i and u_j correspond to solution values associated to the P^1 degrees of freedom (vertices), and to the extra P^2 ones (edge mid-points). Similarly, $\varphi_i^{P^1}$ and $\varphi_i^{P^2}$ denote the linear and quadratic local shape functions. Both in 2D and in 3D on can easily prove the following relations, which will be useful later on (cf. e.g. [12]) :

$$\begin{cases} \varphi_i^{P^2} = \varphi_i^{P^1}(2\varphi_i^{P^1} - 1) & i \text{ is a vertex} \\ \varphi_k^{P^2} = 4\varphi_i^{P^1}\varphi_j^{P^1} & k \text{ is the midpoint of edge} ij \end{cases} \tag{35}$$

The idea is now to replace the mid-point unknowns by values appropriately defined starting from the known nodal values of the pressure and of its gradient To this purpose, a genuine combination of Taylor expansions and the use of the mixed formulation is employed. Looking at Figure 2, focusing on and edge $[i, j]$, the aim is to define the pressure at the midpoint l using only information stored at nodes i and j. We thus consider a third order truncated Taylor expansion of the pressure along the edge, as well as a second order expansion of the flux:

$$\begin{aligned} p(\boldsymbol{x} + \boldsymbol{\delta x}) =& p(\boldsymbol{x}) + \boldsymbol{\nabla} p(\boldsymbol{x}) \cdot \boldsymbol{\delta x} + \frac{1}{2} \boldsymbol{\delta x}^T \boldsymbol{\mathcal{H}}(p) \boldsymbol{\delta x} + \mathcal{O}(||\boldsymbol{\delta x}||^3) \\ \boldsymbol{\beta}(\boldsymbol{x} + \boldsymbol{\delta x}) =& \boldsymbol{\beta}(\boldsymbol{x}) + (\boldsymbol{\nabla} \boldsymbol{\beta}(\boldsymbol{x})) \boldsymbol{\delta x} + \mathcal{O}(||\boldsymbol{\delta x}||^2) \end{aligned} \tag{36}$$

where $\boldsymbol{\mathcal{H}}$ denotes the Hessian of the pressure.

Remark 2. *In this section, the use of the Taylor expansion is not related to the ones performed for the SB method. In equation (36),* $\boldsymbol{\delta x}$ *is thus not linked to the vector distance* $\boldsymbol{d}$ *defined in Section 4 to perform the mapping from the true boundary to the surrogate one.*

If one consider the expression (36) with linear approximation, gradients are constant and the Hessian of the pressure is null. However, using the Darcy equation, the gradient of the

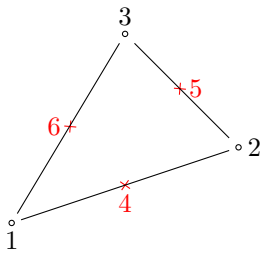

Figure 2: Triangle and additional degrees of freedom (cross nodes)

pressure can be evaluated as $\boldsymbol{\nabla} p = -\frac{1}{\kappa}\boldsymbol{\beta}$ which is actually linear and thus the Hessian can be now evaluated as:

$$\boldsymbol{\mathcal{H}}(p) = -\left[\boldsymbol{\nabla}\left(\boldsymbol{\Lambda^{-1}\beta}\right) + \boldsymbol{\nabla}\left(\boldsymbol{\Lambda^{-1}\beta}\right)^T\right] \tag{37}$$

which is now non null. In the last expression, the superscript ^{T} denotes the transpose of a tensor With this definition, we can easily show that

$$\boldsymbol{\delta x}^T \boldsymbol{\mathcal{H}}(p)\boldsymbol{\delta x} = -\boldsymbol{\delta x}^T \boldsymbol{\nabla}\left(\boldsymbol{\Lambda^{-1}\beta}\right)\boldsymbol{\delta x}$$

The Taylor expansions (36) can thus be rewritten as:

$$\begin{aligned} p(\boldsymbol{x}+\boldsymbol{\delta x}) \approx & p(\boldsymbol{x}) - \boldsymbol{\Lambda^{-1}\beta}\cdot\boldsymbol{\delta x} - \frac{1}{2}\boldsymbol{\delta x}^T\boldsymbol{\nabla}(\boldsymbol{\Lambda^{-1}\beta})\boldsymbol{\delta x} \\ \left(\boldsymbol{\Lambda^{-1}\beta}\right)(\boldsymbol{x}+\boldsymbol{\delta x}) \approx & \left(\boldsymbol{\Lambda^{-1}\beta}\right)(\boldsymbol{x}) + \boldsymbol{\nabla}\left(\boldsymbol{\Lambda^{-1}\beta}\right)(\boldsymbol{x})\boldsymbol{\delta x} \end{aligned} \tag{38}$$

By denoting $\boldsymbol{e}_{i\to j} = \boldsymbol{x}_j - \boldsymbol{x}_i$ the edge vector, the Taylor expansion on the entire edge of $\frac{1}{\kappa}\boldsymbol{\beta}$ gives:

$$\boldsymbol{\nabla}\left(\boldsymbol{\Lambda^{-1}\beta}\right)(\boldsymbol{x})\boldsymbol{e}_{i\to j} = \boldsymbol{\Lambda_j^{-1}\beta}_j - \boldsymbol{\Lambda_i^{-1}\beta}_i \tag{39}$$

By applying the expansion on both node i and j, and, for symmetry reasons, taking the average, we end up with the following estimate for the edge mid-point values:

$$p_l = \overline{p}^e + \frac{1}{8}(\boldsymbol{\Lambda_j^{-1}\beta}_j - \boldsymbol{\Lambda_i^{-1}\beta}_i)\cdot(\boldsymbol{x}_j - \boldsymbol{x}_i) \tag{40}$$

where $\overline{p}^e = \frac{1}{2}(p_j + p_i)$ is the average pressure on the edge. Feeding this expression back to the P^2 approximation, and using (35), one obtains after a few manipulations:

$$p^K(\boldsymbol{x}) = \sum_i p_i\varphi_i(\boldsymbol{x}) + \sum_e \frac{1}{2}\Delta(\boldsymbol{\Lambda^{-1}\beta})_e\cdot\Delta\boldsymbol{x}_e\varphi_1^e(\boldsymbol{x})\varphi_2^e(\boldsymbol{x}) \tag{41}$$

where now only P^1 shape functions are involved, and with the second sum over the edges of K containing a remainder of the P^2 correction associated to the product of test functions associated to each node of the edge e. Also, for a given vector $\boldsymbol{t}$, $\Delta\boldsymbol{t}$ denotes the difference of its values at edge nodes.

Remark 3. *The definition of the enrichment (41) is also valid for tetrahedra.*

6.2 Modification of the schemes

To fully take advantage of the quadratic approximation of the pressure, the boundary conditions also need to be appropriately enhanced for better consistency. In the embedded case, this will require a higher order extrapolation. However, also in the conformal case, some additional conditions are necessary. Indeed, as we are not solving for the mid-point values, some extra information must be imposed to proved a correct behaviour of the pressure enrichment along boundary edges. This has been realized in [30, 37] which propose to inclue on Dirichled boundaries a condition on the tangent variation of the flux, namely

$$< \boldsymbol{w}\cdot\boldsymbol{\tau_i}, \alpha_\tau \left(\frac{1}{\kappa}\boldsymbol{\beta}\cdot\boldsymbol{\tau_i} + \partial_{\tau_i} p_D \right) >_{\Gamma_D} \tag{42}$$

where τ_i denotes the tangent of the boundary in the i direction, and $\partial_{\tau_i} p_D = \boldsymbol{\nabla} p_D \cdot \boldsymbol{\tau}_i$ is the gradient of the Dirichlet value along the boundary. The penalty coefficient α_τ is defined as $\alpha_\tau = \tilde{\alpha} h/||\boldsymbol{\Lambda}||$. The effect of having this term will be tested later in the results section.

We now propose to define the new schemes using the pressure enrichment. In the following, the notation p^* will be employed for the enriched pressure (41).

6.2.1 Conformal case

The conformal case is straightforward. In the scheme (21), for each term involving the pressure, the enrichment (41) is used, and the extra penalty term (42) is employed:

$$\begin{aligned}
B_d(\boldsymbol{w},q;\boldsymbol{\beta},p^*) &= B_d^{Gal}(\boldsymbol{w},q;\boldsymbol{\beta},p^*) + B^{Stab}(\boldsymbol{w},q;\boldsymbol{\beta},p^*) = L_d^{Gal}(\boldsymbol{w},q) + L^{Stab}(\boldsymbol{w},q) \\
B_d^{Gal}(\boldsymbol{w},q;\boldsymbol{\beta},p^*) &= (\boldsymbol{w},\boldsymbol{\Lambda^{-1}}\boldsymbol{\beta})_\Omega - (\boldsymbol{\nabla}\cdot\boldsymbol{w},p^*)_\Omega + (q,\boldsymbol{\nabla}\cdot\boldsymbol{\beta})_\Omega \\
&\quad + < [\![\boldsymbol{w}]\!], \{p^*\} >_{\epsilon_i} - < \{q\}, [\![\boldsymbol{\beta}]\!] >_{\epsilon_i} + < [\![q]\!], \alpha_\beta [\![p^*]\!] >_{\epsilon_i} + < [\![\boldsymbol{w}]\!], \alpha_p [\![\boldsymbol{\beta}]\!] >_{\mathcal{E}_i} \\
&\quad + < \boldsymbol{w}\cdot\boldsymbol{n}, p^* >_{\Gamma_N} - < q, \boldsymbol{\beta}\cdot\boldsymbol{n} >_{\Gamma_N} + < q, \alpha_\beta p^* >_{\Gamma_D} + < \boldsymbol{w}\cdot\boldsymbol{\tau_i}, \alpha_\tau \frac{1}{\kappa}\boldsymbol{\beta}\cdot\boldsymbol{\tau_i} >_{\Gamma_D} \\
L_d^{Gal}(\boldsymbol{w},q) &= (q,\phi)_\Omega - < \boldsymbol{w}\cdot\boldsymbol{n}, p_D >_{\Gamma_D} + < q, \alpha_\beta p_D >_{\Gamma_D} - < q, h_N >_{\Gamma_N} - < \boldsymbol{w}\cdot\boldsymbol{\tau_i}, \alpha_\tau \partial_{\tau_i} p_D >_{\Gamma_D}
\end{aligned} \tag{43}$$

The test functions employed are still linear, $(\boldsymbol{w},q) \in S^1(\Omega)\times\boldsymbol{V}^1(\Omega)$. However, the enriched pressure p^* is defined to be a quadratic approximation of the pressure, therefore, $p^* \in S^2(\Omega)$. As recalled in section 5, with the error estimate (23), if $(\boldsymbol{\beta},p) \in \boldsymbol{V}^k(\Omega)\times S^l(\Omega)$, with $r = \min(k+1,l)$, the expected convergence rate is of order r and $r+1$ for the flux and pressure respectively. Consequently, with the enrichment, the new expected convergence rates are a second order flux and third order pressure.

In addition, the enrichment performing a quadratic approximation of the pressure, it is expected that the resulting scheme would recover up to machine precision quadratic exact solutions of the Darcy flow problem (1).

6.2.2 Embedded case: third order extrapolation

For the embedded case, to be consistent with the internal approximation of the pressure, the boundary terms of the type $< q, \alpha_\beta(p-p_D) >_{\Gamma_D} + < \boldsymbol{w}\cdot\boldsymbol{n}, p_D >_{\Gamma_D}$ need to be modified to account for a parabolic extrapolation. For this reason when extending the value of the pressure from the true boundary Γ_D onto the surrogate one $\tilde{\Gamma}_D$, the Taylor expansion (29) has bee enhanced as:

$$p_D(\boldsymbol{x}) = \overline{p}_D = p_D(\tilde{\boldsymbol{x}}) + \boldsymbol{\nabla} p\cdot\boldsymbol{d} + \frac{1}{2}\boldsymbol{d}^T\boldsymbol{\mathcal{H}}(p)\boldsymbol{d} \tag{44}$$

which involves the Hessian of the pressure. As done on internal edges, to evaluate the Hessian we use the nodal flux, which essentially leads to (38) with $\boldsymbol{\delta x} = \boldsymbol{d}$. The resulting shifted boundary condition reads:

$$p_D(\boldsymbol{x}) = \bar{p}_D = p_D(\tilde{\boldsymbol{x}}) - (\boldsymbol{\Lambda^{-1}\beta}) \cdot \boldsymbol{d} - \frac{1}{2}\boldsymbol{d}^T \boldsymbol{\nabla} \left(\boldsymbol{\Lambda^{-1}\beta}\right) \boldsymbol{d} \tag{45}$$

Thus, the Dirichlet terms are now modified as follows:

$$< q - \boldsymbol{\Lambda^{-1}w}\cdot\boldsymbol{d} - \frac{1}{2}\boldsymbol{d}^T\boldsymbol{\nabla}\left(\boldsymbol{\Lambda^{-1}w}\right)\boldsymbol{d}, \alpha(p - \boldsymbol{\Lambda^{-1}\beta}\cdot\boldsymbol{d} - \frac{1}{2}\boldsymbol{d}^T\boldsymbol{\nabla}\left(\boldsymbol{\Lambda^{-1}\beta}\right)\boldsymbol{d} - \bar{p}_D) >_{\tilde{\Gamma}_D} + < \boldsymbol{w}\cdot\tilde{\boldsymbol{n}}, \boldsymbol{\Lambda^{-1}\beta}\cdot\boldsymbol{d} + \frac{1}{2}\boldsymbol{d}^T\boldsymbol{\nabla}\left(\boldsymbol{\Lambda^{-1}\beta}\right)\boldsymbol{d} + \bar{p}_D >_{\tilde{\Gamma}} \tag{46}$$

where the expression in the left slot is designed to guarantee the symmetry as well as de positive semi-definiteness of the associated variational form, in the spirit of the formulation used in [27].

The extra high order correction on the gradient in the tangential direction is also extended using the Taylor expansion:

$$\partial_{\tau_i}\bar{p}_D = \boldsymbol{\nabla}\bar{p}_D \cdot \boldsymbol{\tau}_i = \boldsymbol{\Lambda^{-1}\beta}(\tilde{\boldsymbol{x}})\cdot\boldsymbol{\tau}_i + \boldsymbol{\nabla}\left(\boldsymbol{\Lambda^{-1}\beta}\right)\boldsymbol{d}\cdot\boldsymbol{\tau}_i + \mathcal{O}(||\boldsymbol{d}||^2) \tag{47}$$

As no modification is performed on the flux itself, the Neumann boundary terms remain unchanged. Thus, The final embedded formulation using pressure enrichment finally writes:

$$\begin{aligned}
B_d(\boldsymbol{w},q;\boldsymbol{\beta},p^*) &= B_d^{Gal}(\boldsymbol{w},q;\boldsymbol{\beta},p^*) + B^{Stab}(\boldsymbol{w},q;\boldsymbol{\beta},p^*) = L_d^{Gal}(\boldsymbol{w},q) + L^{Stab}(\boldsymbol{w},q)\\
B_d^{Gal}(\boldsymbol{w},q;\boldsymbol{\beta},p^*) &= (\boldsymbol{w},\boldsymbol{\Lambda^{-1}\beta})_{\tilde{\Omega}} - (\boldsymbol{\nabla}\cdot\boldsymbol{w},p^*)_{\tilde{\Omega}} + (q,\boldsymbol{\nabla}\cdot\boldsymbol{\beta})_{\tilde{\Omega}}\\
&+ < [\![\boldsymbol{w}]\!], \{p^*\} >_{\epsilon_i} - < \{q\}, [\![\boldsymbol{\beta}]\!] >_{\epsilon_i} + < [\![q]\!], \alpha_\beta [\![p^*]\!] >_{\epsilon_i} + < [\![\boldsymbol{w}]\!], \alpha_p [\![\boldsymbol{\beta}]\!] >_{\mathcal{E}_i}\\
&+ < (\boldsymbol{w} + [\boldsymbol{\nabla w}]\boldsymbol{d})\cdot\boldsymbol{\tau_i}, \alpha_\tau(\boldsymbol{\Lambda^{-1}\beta} + [\boldsymbol{\nabla}\left(\boldsymbol{\Lambda^{-1}\beta}\right)]\boldsymbol{d})\cdot\boldsymbol{\tau}_i >_{\tilde{\Gamma}_D} + < \boldsymbol{w}\cdot\tilde{\boldsymbol{n}}, \boldsymbol{\Lambda^{-1}\beta}\cdot\boldsymbol{d} + \frac{1}{2}\boldsymbol{d}^T\boldsymbol{\nabla}\left(\boldsymbol{\Lambda^{-1}\beta}\right)\boldsymbol{d} >_{\tilde{\Gamma}_D}\\
&+ < q - \boldsymbol{\Lambda^{-1}w}\cdot\boldsymbol{d} - \frac{1}{2}\boldsymbol{d}^T\boldsymbol{\nabla}\left(\boldsymbol{\Lambda^{-1}w}\right)\boldsymbol{d}, \alpha_\beta(p - \frac{1}{\kappa}\boldsymbol{\beta}\cdot\boldsymbol{d} - \frac{1}{2}\boldsymbol{d}^T\boldsymbol{\nabla}\left(\boldsymbol{\Lambda^{-1}\beta}\right)\boldsymbol{d}) >_{\tilde{\Gamma}_D}\\
&+ < \boldsymbol{w}\cdot\tilde{\boldsymbol{n}}, p^* >_{\tilde{\Gamma}_N} - < q(\boldsymbol{n}\cdot\tilde{\boldsymbol{n}}), (\boldsymbol{\beta} + [\boldsymbol{\nabla\beta}]\boldsymbol{d})\cdot\boldsymbol{n} >_{\tilde{\Gamma}_N}\\
L_d^{Gal}(\boldsymbol{w},q) &= (q,\phi)_{\tilde{\Omega}} - < q(\boldsymbol{n}\cdot\tilde{\boldsymbol{n}}), \bar{h}_N >_{\tilde{\Gamma}_N} - < \boldsymbol{w}\cdot\tilde{\boldsymbol{n}}, \bar{p}_D >_{\tilde{\Gamma}_D} + < q - \boldsymbol{\Lambda^{-1}w}\cdot\boldsymbol{d} - \frac{1}{2}\boldsymbol{d}^T\boldsymbol{\nabla}\left(\boldsymbol{\Lambda^{-1}w}\right)\boldsymbol{d}, \alpha_\beta\bar{p}_D >_{\tilde{\Gamma}_D}\\
&- < (\boldsymbol{w} + [\boldsymbol{\nabla w}]\boldsymbol{d})\cdot\boldsymbol{\tau_i}, \alpha_\tau\partial_{\tau_i}\bar{p}_D >_{\tilde{\Gamma}_D}
\end{aligned} \tag{48}$$

As before, the continuous Galerkin formulation is obtained by cancelling all internal edge integrals involving jumps. The expression is omitted for brevity. The Euler-Lagrange equations associated to the enriched scheme read:

$$\begin{aligned}
&(\boldsymbol{w}, (\boldsymbol{\Lambda^{-1}\beta} + \boldsymbol{\nabla}p^*))_{\tilde{\Omega}} + (q, (\boldsymbol{\nabla}\cdot\boldsymbol{\beta} - \phi))_{\tilde{\Omega}}\\
&- < \boldsymbol{w}\cdot\tilde{\boldsymbol{n}} + \alpha_\beta(q - \boldsymbol{\Lambda^{-1}w}\cdot\boldsymbol{d} - \frac{1}{2}\boldsymbol{d}^T\boldsymbol{\nabla}\left(\boldsymbol{\Lambda^{-1}w}\right)\boldsymbol{d}), p^* - \boldsymbol{\Lambda^{-1}\beta}\cdot\boldsymbol{d} - \frac{1}{2}\boldsymbol{d}^T\boldsymbol{\nabla}\left(\boldsymbol{\Lambda^{-1}\beta}\right)\boldsymbol{d} - \bar{p}_D >_{\tilde{\Gamma}_D}\\
&+ < (\boldsymbol{w} + [\boldsymbol{\nabla w}]\boldsymbol{d})\cdot\boldsymbol{\tau}_i, \alpha_\tau\left(\boldsymbol{\Lambda^{-1}\beta} + \left[\boldsymbol{\nabla}\left(\boldsymbol{\Lambda^{-1}\beta}\right)\right]\boldsymbol{d}\right)\cdot\boldsymbol{\tau}_i - \partial_{\tau_i}\bar{p}_D >_{\tilde{\Gamma}_D}\\
&- < q(\boldsymbol{n}\cdot\tilde{\boldsymbol{n}}), (\boldsymbol{\beta} + (\boldsymbol{\nabla\beta})\boldsymbol{d})\cdot\boldsymbol{n} - \bar{h}_N >_{\tilde{\Gamma}_N} = 0
\end{aligned} \tag{49}$$

This Euler-Lagrange formulation differs from the original one (33) by the use of the enriched pressure, and due to the modified Dirichlet boundary conditions. On $\tilde{\Gamma}_D$, to enforce with higher accuracy the boundary condition, the Taylor expansion is pushed to third order, and the extra high order correction of the gradient in the tangential direction is added and shifted. Such a scheme, as will be illustrated in the next Section devoted to numerical applications, allows to recover an overall second order accuracy.

Remark 4. *The extrapolation of the pressure could be already pushed to third order without the pressure enrichment. However, such a procedure is unnecessary as the expected accuracy is 2 and already satisfied by a second order Taylor expansion.*

Remark 5. *We stress one more that the use of the enrichment does not require the insertion of additional degrees of freedom or new equations. However, additional terms are added to the weak formulation.*

7 Results

In this section, we demonstrate the effectiveness of the method proposed on several numerical examples. First we consider two dimensional $2D$ convergence tests for both conformal and embedded simulations. For sake of completeness, two problems are considered, one involving an isotropic spatially dependent permeability, and the second one presenting a constant anisotropic permeability matrix. Then we study more specifically the embedded case for which we show the capability of the method to recover exactly linear and quadratic solutions (with pressure enrichment) using some patch tests, with continuous and discontinuous solutions. To complete the $2D$ tests, we compare the embedded and conformal solutions for flow in a domain with an impermeability circular obstruction and flow in a domain with low permeability obstruction.

Finally, we propose some results in $3D$, and in particular a $3D$ convergence test as well as an example of a flow computation around a complex $3D$ shape with slip wall (Neumann) conditions.

For all $2D$ and $3D$ simulations, the Dirichlet penalty coefficients have been set to $\alpha_p = \alpha_\tau = 2$, and $\alpha_\beta = 0$ for convergence tests and $\alpha_\beta = 0.5$ for the other tests. Regarding the ζ constant present in the stabilization [29], it has been used $\zeta = 0.5$.

7.1 Convergence tests

This first convergence tests aim at showing that the expected convergence rates are recovered numerically, with a analysis of the cost of the pressure enrichment. In addition, we also illustrate the influence of the penalty term on the tangential flux for Dirichlet condition when the enrichment is employed.

7.1.1 Presentation of the tests cases

So as to validate the proposed method, we start by checking the convergence rates. The solutions employed for this study are defined as:

$$\begin{cases} \boldsymbol{\beta}(x,y) = \begin{pmatrix} -e^{x+y}(x^2+y) \\ -e^{x+y}(x+y^2) \end{pmatrix} \\ p(x,y) = \dfrac{1}{3}(x^3+y^3) + xy \\ \phi(x,y) = -(y^2+x^2+3x+3y)e^{x+y} \\ \boldsymbol{\Lambda} = e^{x+y}\mathbb{I} \end{cases} \tag{50}$$

for the variable permeability, and:

$$\left\{\begin{array}{l} \boldsymbol{\beta}(x,y) = \left(\begin{array}{l} 2\lambda_{xy}\pi\cos(2\pi x)\sin(2\pi x)\sin^2(2\pi y) + (2\lambda_{xx}\pi\sin^2(2\pi x) - 2\lambda_{xx}\pi\cos^2(2\pi x))\cos(2\pi y)\sin(2\pi y) \\ -2\lambda_{xy}\pi\cos(2\pi x)\sin(2\pi x)\cos^2(\pi y) \\ 2\lambda_{yy}\pi\cos(2\pi x)\sin(2\pi x)\sin^2(2\pi y) + (2\lambda_{yx}\pi\sin^2(2\pi x) - 2\lambda_{yx}\pi\cos^2(2\pi x))\cos(2\pi y)\sin(2\pi y) \\ -2\lambda_{yy}\pi\cos(2\pi x)\sin(2\pi x)\cos^2(2\pi y) \end{array}\right) \\ p(x,y) = \cos(2\pi x)\sin(2\pi x)\cos(2\pi y)\sin(2\pi y) \\ \phi(x,y) = 4(\lambda_{yx}+\lambda_{xy})\pi^2(\sin^2(2\pi x) - \cos^2(2\pi x))(\cos(2\pi y)^2 - \sin^2(2\pi y)) \\ \qquad + (16\lambda_{yy} + 16\lambda_{xx})\pi^2\cos(2\pi x)\sin(2\pi x)\cos(2\pi y)\sin(2\pi y) \\ \qquad \boldsymbol{\Lambda} = \left[\begin{array}{cc} \lambda_{xx} & \lambda_{xy} \\ \lambda_{yx} & \lambda_{yy} \end{array}\right] = \left[\begin{array}{cc} 3 & 1 \\ 1 & 3 \end{array}\right] \end{array}\right. \tag{51}$$

for the anisotropic permeability.

7.1.2 Conformal Results

Here we propose to verify that the proposed approach allows to recover the expected convergence rates for conformal simulations. The tests are performed on a domain defined by two circles of radius $r_{out} = 0.35$ and $r_{in} = 0.1$ on which are imposed respectively Dirichlet and Neumann conditions (see Figure 3(a)). For the variable permeability (50), convergence rates for both discontinuous and continuous discretizations are given on Figure 4(a) for the flux and Figure 4(b) for the pressure. For the anisotropic one (51), convergence rates for both discontinuous and continuous discretizations are given on Figure 4(c) for the flux and Figure 4(d) for the pressure. One can easily appreciate that the plots match the expected convergence rates: with the original formulation a second order pressure and first order flux are recovered while the use of the enriched pressure allows to get a third order pressure and a second order flux. Those convergences are similar to the ones obtained in [18] with unequal order elements, where the pressure is discretized with P_2 degrees of freedom and velocity P_1. However, in the present study, both variables are discretized using P_1 degrees of freedom. A reduced number of degrees of freedom allows to recover the same accuracy.

7.1.3 Embedded results

The setup for the embedded convergence studies is the following: the two circles of radius $r_{in} = 0.1$ and $r_{out} = 0.35$ are embedded in a bigger domain, as depicted Figure 3(b). In a first time, Dirichlet conditions are applied on both inner and outer radius to check the convergence rates of embedded Dirichlet conditions. Such test cases will be denoted by *Dirichlet/Dirichlet*. Secondly, while keeping a Dirichlet on the outer embedded circle, we apply a Neumann condition on the inner circle. This setting will be denominated *Neumann/Dirichlet*.
Plots of the solutions (with variable permeability) on the surrogate domain are displayed on Figure 5. For the Dirichlet/Dirichlet simulations, convergence rates obtained with the isotropic solution for both CG and DG schemes are provided on Figure 6(a) and 6(b) for respectively flux and pressure. The anisotropic results are plotted on Figure 6(c) for the flux and on Figure 6(d) for the pressure. The convergence rates corresponding to the Neumann/Dirichlet are given for isotropic variable permeability on Figure 7(a) for the flux and on Figure 7(b) for the pressurel, and Figures 7(c) and 7(d) for the anisotropic convergence rates. Those plots match the expected convergence rates. When the pressure enrichment is activated, in both cases, the flux is second

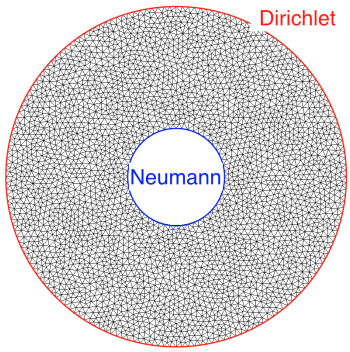

(a) Conformal simulation domain and mesh

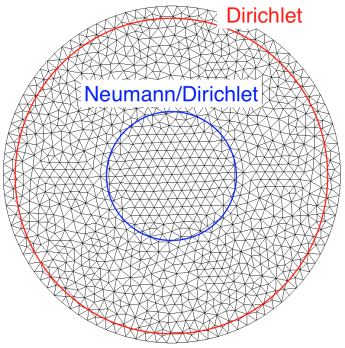

(b) Embedded simulation domain and mesh

Figure 3: Convergence test cases configurations

order accurate, and the pressure is third order accurate for pure Dirichlet and second order accurate for Neumann boundary condition. We thus validate our approach to provide high order flux and pressure for any kind of boundary condition, and the gain of one order of accuracy for both variables using the pressure enrichment.

We are now interested by the gain provided by the pressure enrichment. The condition number as a function of the mesh size is proposed on Figure 8. We can see that the use of the enrichment has a minimum influence on the condition number, demonstrating that this enrichment is not impacting the conditioning of the matrix.

7.1.4 On the influence of the tangential penalty

As explained previously, the additional penalty term is mainly present so as to enhance stability and accuracy when the pressure enrichment is employed. If not used, some spurious modes can be observed. We devote this small paragraph to illustrate this phenomena. We perform, on the same mesh, the simulations with respectively $\alpha_\tau = 0$ and 2. Plots of the solutions close to the inner circle are provided Figure 9(a) for conformal simulation with the anisotropic permeability and Figure 9(b) for embedded simulation wit variable permeability. One can appreciate the loss of those spurious modes with the add of this extra penalty term.

7.2 Patch test cases

We now tackle the problem of approximating exactly polynomial solutions of the same degree than the space of approximation. To this purpose, we propose to perform the same analysis than in [35] involving discontinuous viscosities

$$\kappa(x,y) = \begin{cases} \kappa_1 & \text{if } x \leq 0.5 \\ \kappa_2 & \text{if } x > 0.5 \end{cases} \tag{52}$$

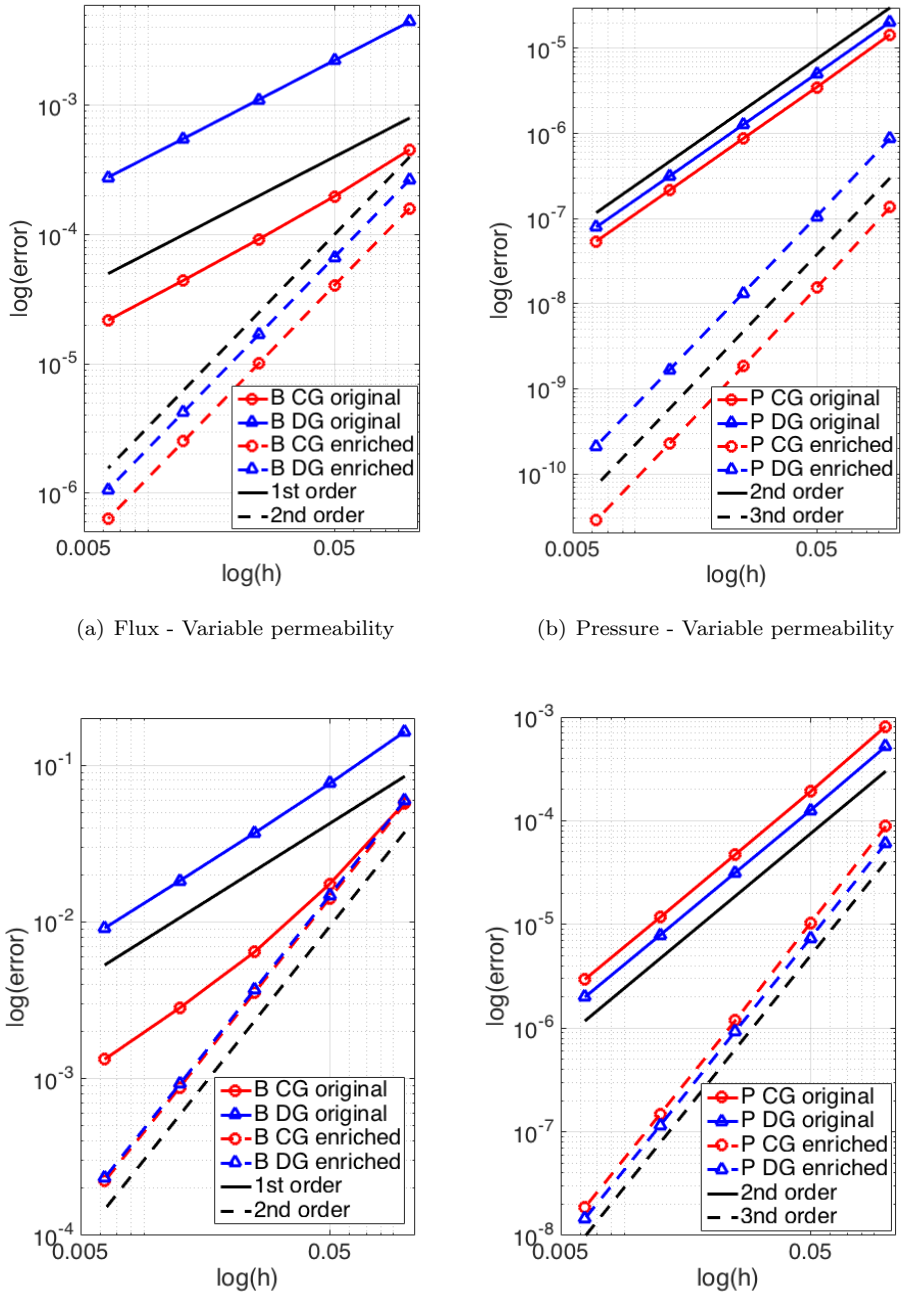

(a) Flux - Variable permeability

(b) Pressure - Variable permeability

(c) Flux - Anosotropic permeability

(d) Pressure - Anisotropic permeability

Figure 4: Convergence test - Conformal case

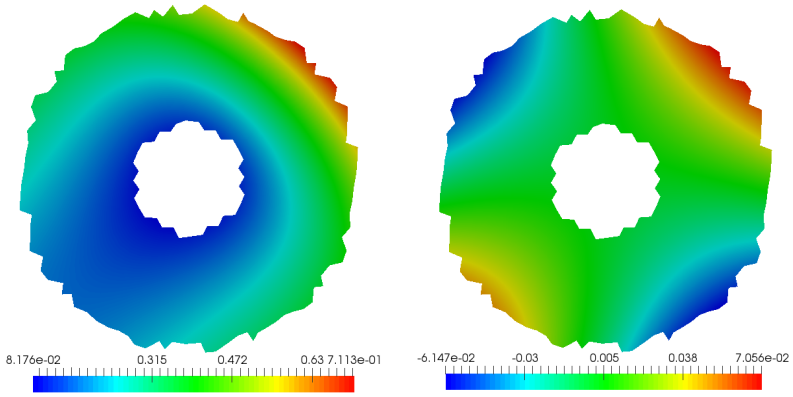

(a) Flux norm (b) Pressure

Figure 5: Convergence test - Plots of the solution - Variable permeability

The two studied solutions are taken from [35] and generalized to any polynomial degree r. They are defined as:

$$\begin{cases} p_{CG}(x,y) = \begin{cases} \frac{1}{\tilde{\kappa}}\left(\frac{1}{r}\kappa_2 x^r + 2\kappa_1\kappa_2\right) & \text{if } x \leq 0.5 \\ \frac{1}{\tilde{\kappa}}\left(\frac{1}{r}\kappa_1 x^r + 2\kappa_1\kappa_2 + \frac{1}{r2^r}(\kappa_2 - \kappa_1)\right) & \text{if } x > 0.5 \end{cases} \\ \boldsymbol{\beta}_{CG}(x,y) = \begin{cases} -\frac{\kappa_1\kappa_2 x^{r-1}}{\tilde{\kappa}} \\ 0 \end{cases} \\ \phi(x,y)_{CG} = -(r-1)\frac{\kappa_1\kappa_2 x^{r-2}}{\tilde{\kappa}} \end{cases} \tag{53}$$

where $\tilde{\kappa} = 0.5(\kappa_1 + \kappa_2) + 4\kappa_1\kappa_2$, and:

$$\begin{cases} p_{DG}(x,y) = \begin{cases} 1 + x^r + y^r & \text{if } x \leq 0.5 \\ 1 + \frac{\kappa_2 - \kappa_1}{2^r\kappa_2} + \frac{\kappa_1}{\kappa_2}x^r + y^r & \text{if } x > 0.5 \end{cases} \\ \beta_{x,DG}(x,y) = -\kappa_1 r x^{r-1} \\ \beta_{y,DG}(x,y) = \begin{cases} -\kappa_1 r y^{r-1} & \text{if } x \leq 0.5 \\ -\kappa_2 r y^{r-1} & \text{if } x > 0.5 \end{cases} \\ \phi_{DG}(x,y) = \begin{cases} -\kappa_1 r(r-1)(x^{r-2} + y^{r-2}) & \text{if } x \leq 0.5 \\ -r(r-1)(\kappa_1 x^{r-2} + \kappa_2 y^{r-2}) & \text{if } x \leq 0.5 \end{cases} \end{cases} \tag{54}$$

where for those specific two last equations (53,54), we define $x^\alpha = 0$ if $\alpha < 0$.

Those two test cases present a continuous pressure whom gradient is discontinuous. However, while the solution (53) does not involve discontinuity on the variables themselves , the second one (54) proposes a discontinuous flux. The first setting (53) can thus be used for both continuous and discontinuous schemes while the second one (54) can only be solved exactly using the dicontinuous approximation.

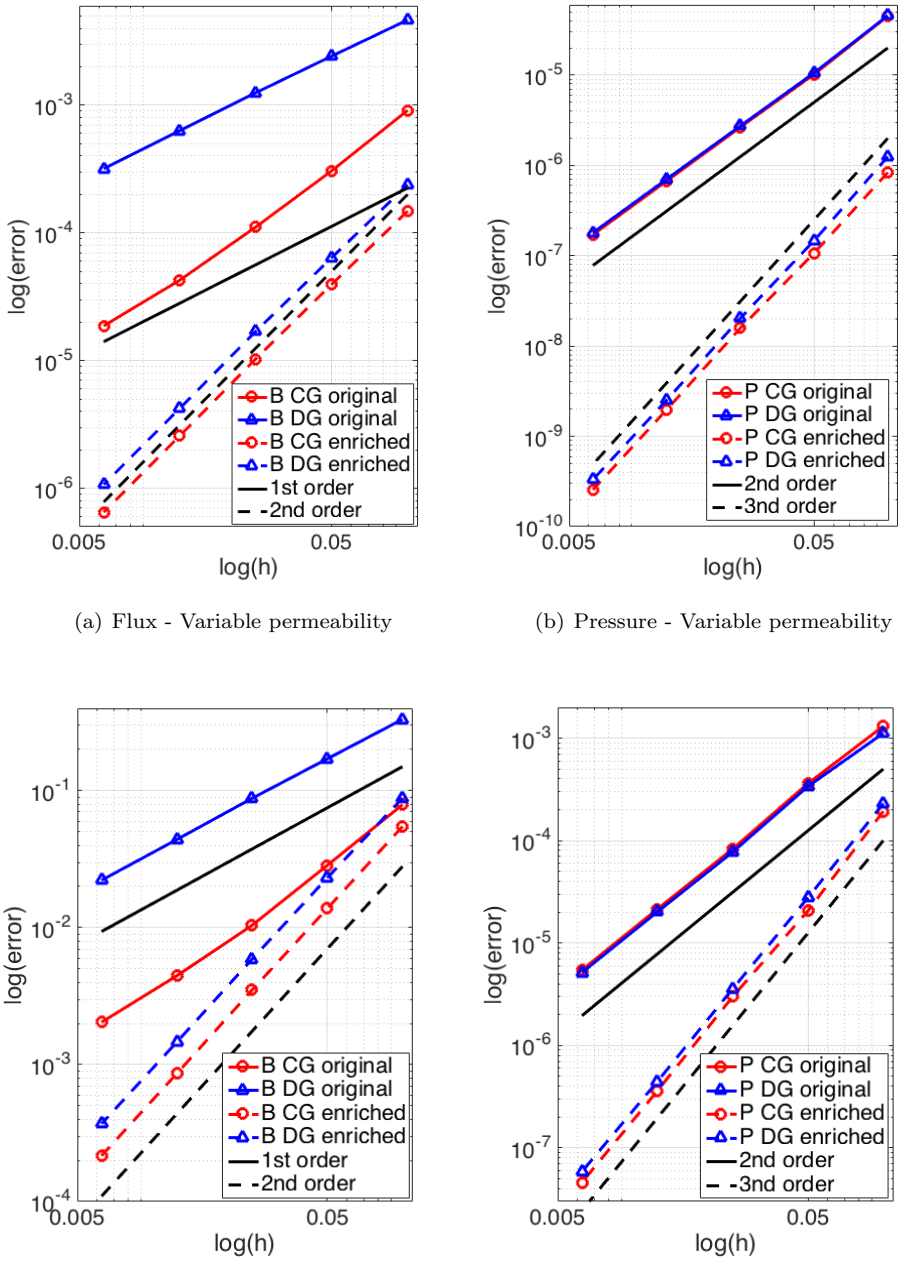

(a) Flux - Variable permeability

(b) Pressure - Variable permeability

(c) Flux - Anisotropic permeability

(d) Pressure - Anisotropic permeability

Figure 6: Convergence test, embedded simulations - Dirichlet/Dirichlet

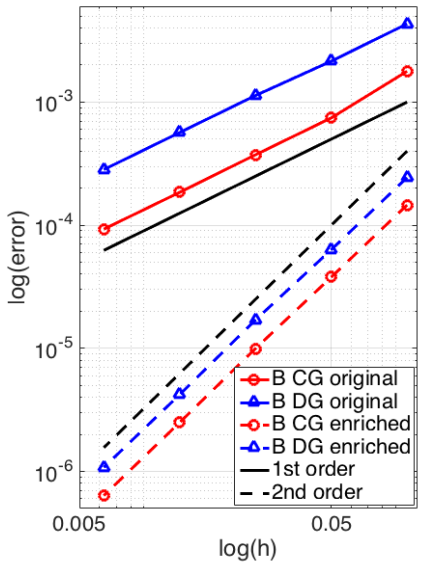

(a) Flux - Variable permeability

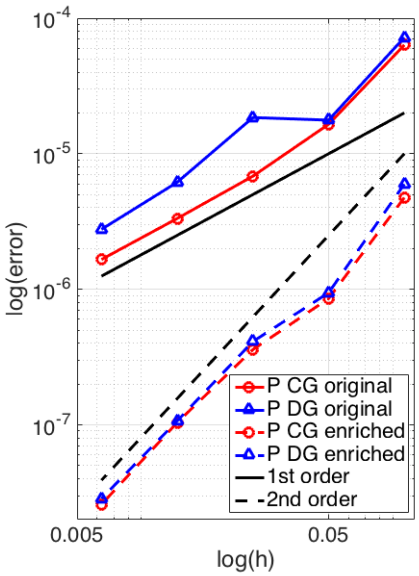

(b) Pressure - Variable permeability

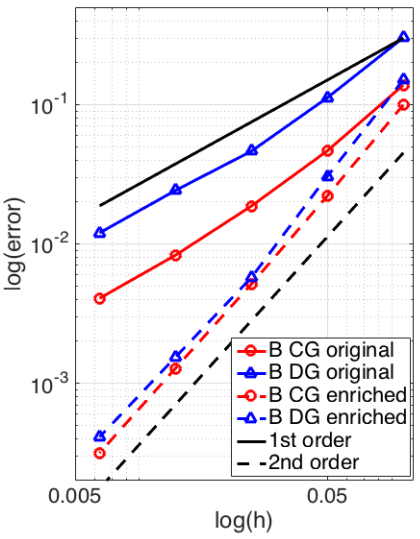

(c) Flux - Anisotropic permeability

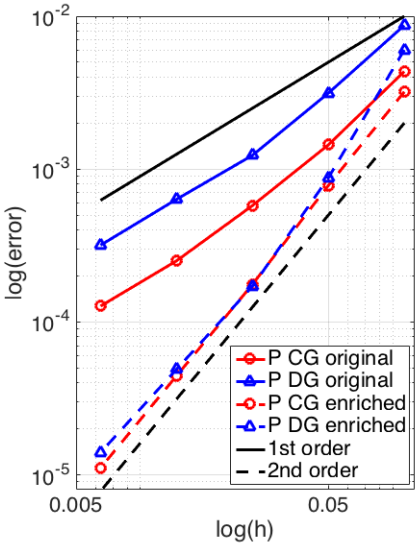

(d) Pressure - Anisotropic permeability

Figure 7: Convergence test, embedded simulations - Neumann/Dirichlet

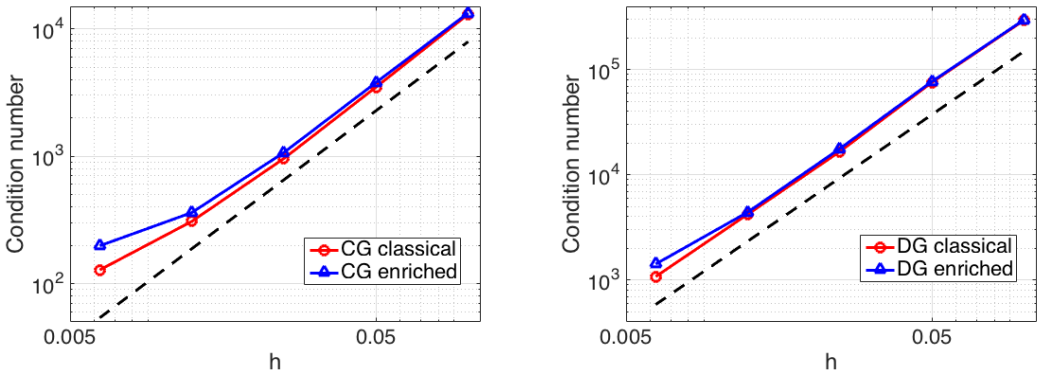

(a) Continuous scheme (b) Discontinuous scheme

Figure 8: Matrix condition number - the dotted line corresponds to the slope h^{-2}.

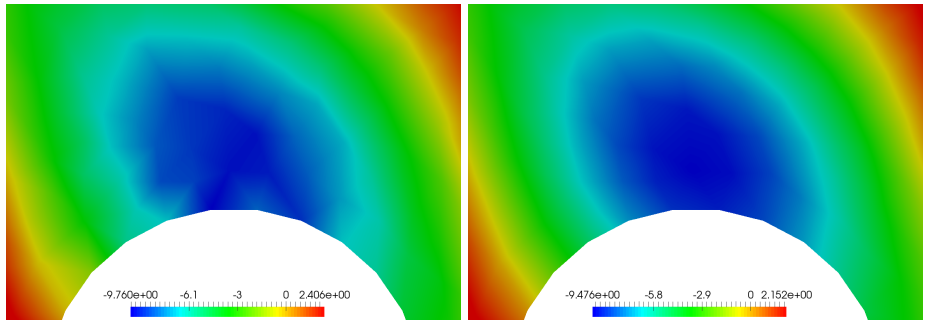

(a) Conformal - Anisotropic permeability. Left: $\alpha_\tau = 0$ - Right: $\alpha_\tau = 2$

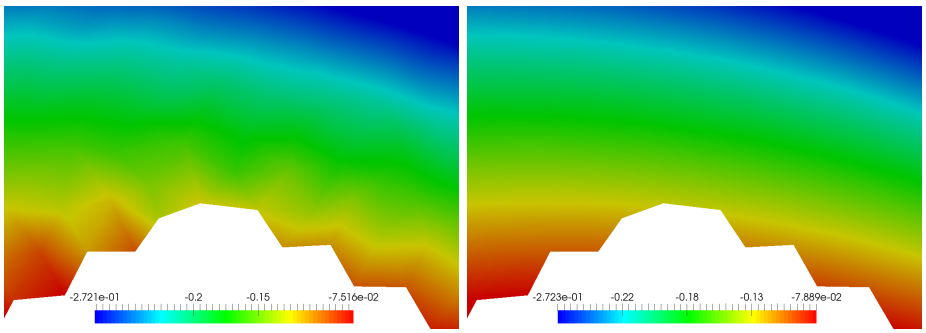

(b) Embedded - Variable permeability. Left: $\alpha_\tau = 0$ - Right: $\alpha_\tau = 2$

Figure 9: Dirichlet boundary condition with pressure enrichment - Influence of the tangential flux penalty term - x component of the flux

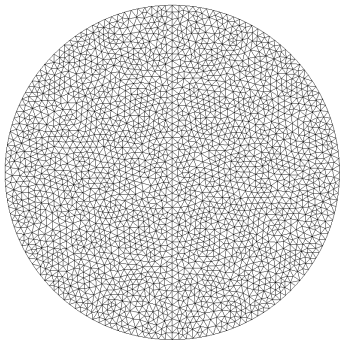

Figure 10: Patch tests mesh

In a circular domain of radius $R = 0.6$, two circles are of radius $r_{in} = 0.1$ and $r_{out} = 0.5$ are embedded on which are respectively imposed Neumann and Dirichlet conditions. The mesh generated is composed of $2,531$ nodes and $4,908$ triangles, with an explicit discretization of the discontinuous line in $x = 0.5$ (see Figure 10). We perform the simulations for a linear pressure / constant flux ($r = 1$) and quadratic pressure / linear flux ($r = 2$) with and without the enrichment.

For $r = 1$, for both CG and DG schemes, plots of the pressure and one component of the flux along with the errors are proposed on Figure 11 for the solution (53). For the second setting (54), the solutions obtained with the discontinuous scheme are proposed on Figure (12). As expected, for the continuous variables, both schemes perfectly match the exact solution. Identically, the discontinuous scheme allows to exactly capture the discontinuous one. For this latest case however, a continuous apporoximation does not allow to properly capture discontinuities, as some spurious oscillations appear close to the interface, as depicted on Figure 13.

Considering now the case $r = 2$, as CG and DG schemes behave identically, we plot only the results obtained with the continuous formulation along with the errors obtained with both original and enriched schemes on Figure 14 for the continuous solution (53). For the discontinuous solution (54), the simulations are only performed with the discontinuous scheme and the results are displayed on Figure 15. On can easily appreciate that while the original CG and DG schemes do not allow to recover an exact approximation of the solutions, the enriched formulations propose a perfect match (up to machine precision) of quadratic solutions.

7.3 A domain with a circular impermeable obstruction

The domain is $[0,1] \times [0,1] \setminus \Omega_0$ where Ω_0 is a circle of radius 0.2 centered in $(0.5, 0.5)$. The permeability in the domain is $\mathbf{\Lambda} = \mathbb{I}$. On the left and right side we apply Dirichlet conditions with respectively $p = 1$ and $p = 0$ while all others boundaries are set to slip wall: $\boldsymbol{\beta} \cdot \boldsymbol{n} = 0$ (see Figure 16(a)). As there is no discontinuity in the permeability, the continuous scheme is employed. We compare the solutions for a conformal simulation and one where the inner impermeable obstruction is embedded. The mesh employed are provided Figures 16(b) and 16(c). Isolines of the flux and pressure are displayed for both simulations on Figure 17(a) and elevation plots of the flux magnitude are compared on Figure 17(b). One can easily appreciate the fact that the solutions are quasi identical.

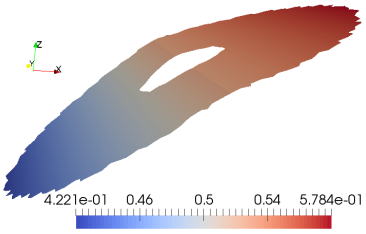

(a) Pressure profile

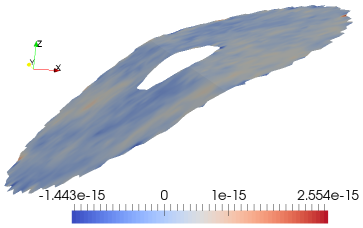

(b) Pressure error - Continuous scheme

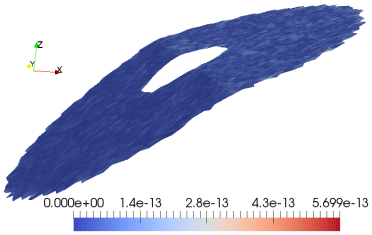

(c) Pressure error - Discontinuous scheme

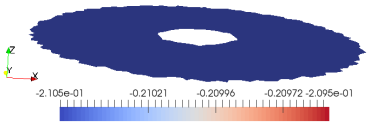

(d) β_x profile

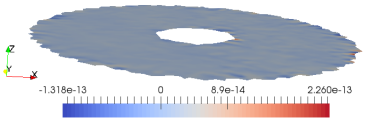

(e) β_x error - Continuous scheme

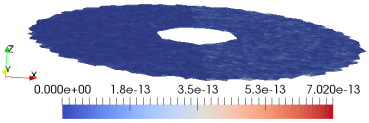

(f) β_x error - Discontinuous scheme

Figure 11: Patch test with CG scheme - Linear pressure and constant flux plotted on elevation plots obtained with the corresponding scheme

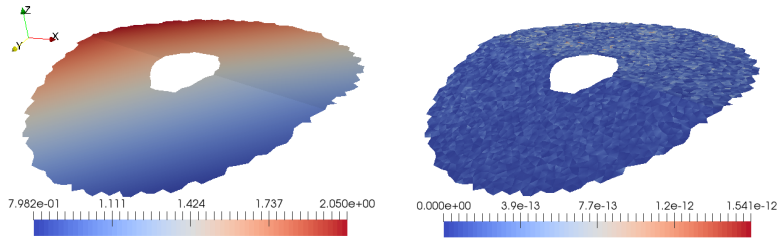

(a) Pressure profile (b) Pressure error

(c) β_y profile (d) β_y error

Figure 12: Patch test with DG scheme - Linear pressure and constant flux plotted on elevation plots obtained with the corresponding scheme

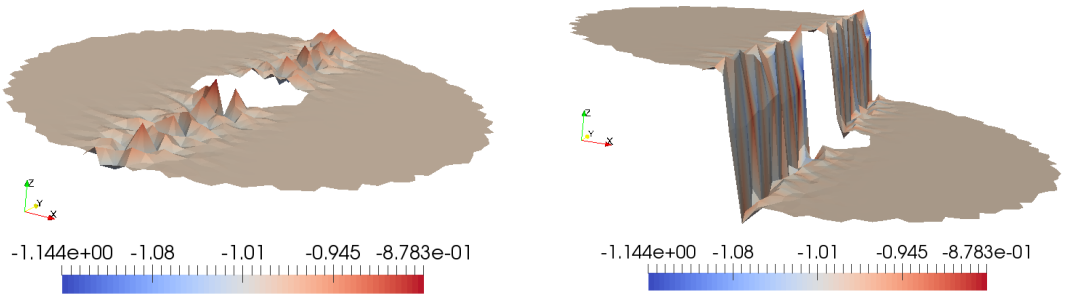

(a) x component (b) x component

Figure 13: Flux obtained with CG scheme for discontinuous solution

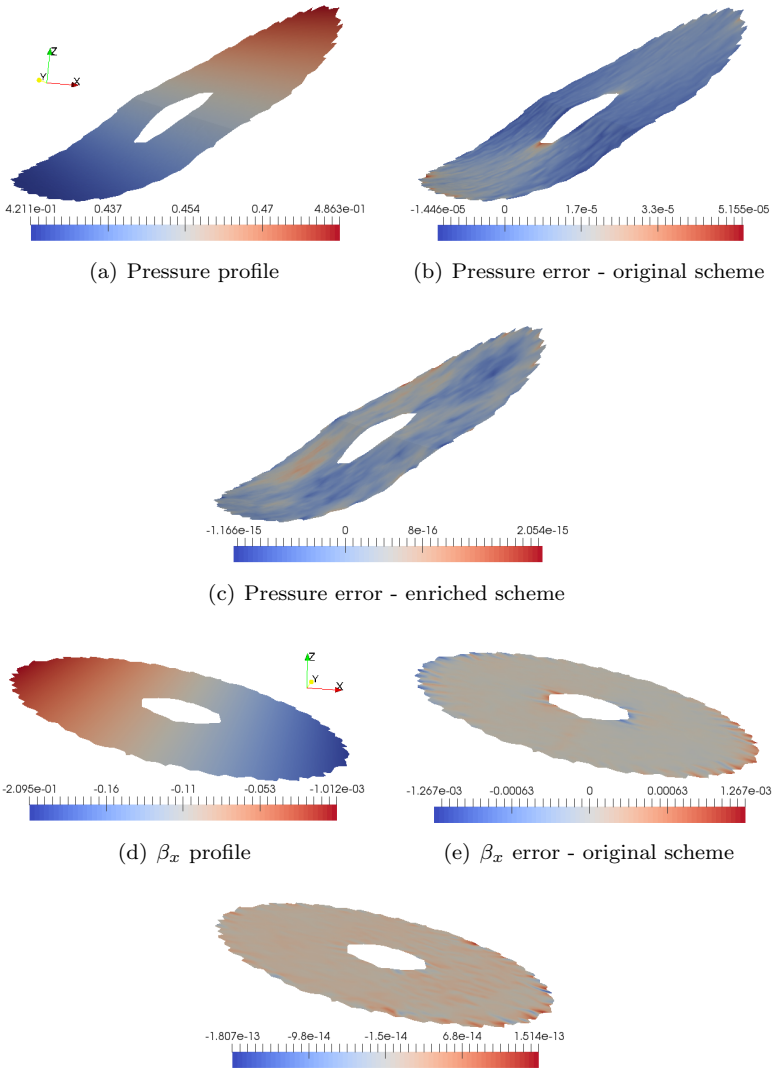

(a) Pressure profile (b) Pressure error - original scheme

(c) Pressure error - enriched scheme

(d) β_x profile (e) β_x error - original scheme

(f) β_x error - enriched scheme

Figure 14: Patch test with CG scheme - Quadratic pressure and linear flux plotted on elevation plots obtained with the corresponding scheme

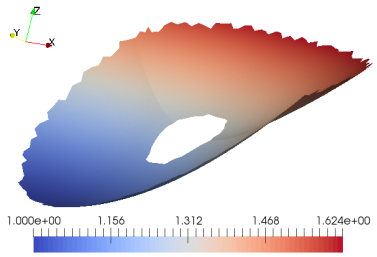

(a) Pressure profile

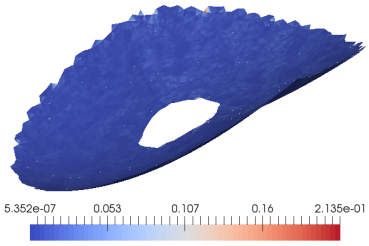

(b) Pressure error - original scheme

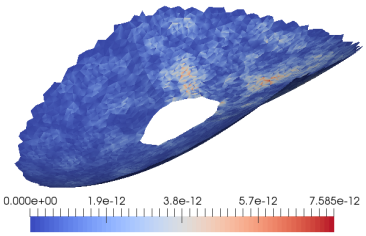

(c) Pressure error - enriched scheme

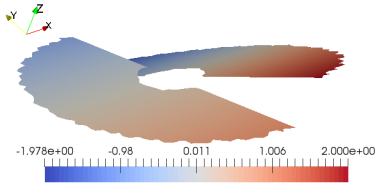

(d) β_y profile

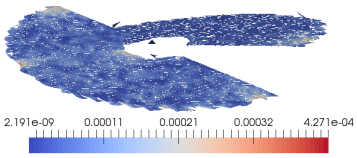

(e) β_y error - original scheme

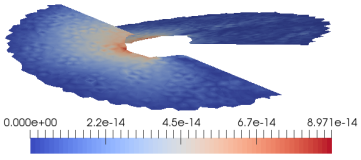

(f) β_y error - enriched scheme

Figure 15: Patch test with DG scheme - Quadratic pressure and linear flux plotted on elevation plots obtained with the corresponding scheme

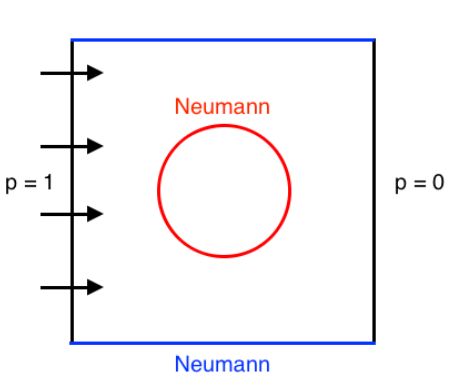

(a) Domain and boundary conditions

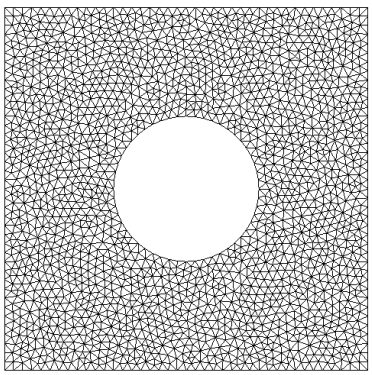

(b) Conformal mesh

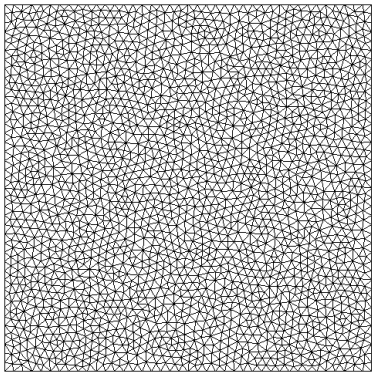

(c) Embedded mesh

Figure 16: Circular impermeable obstruction

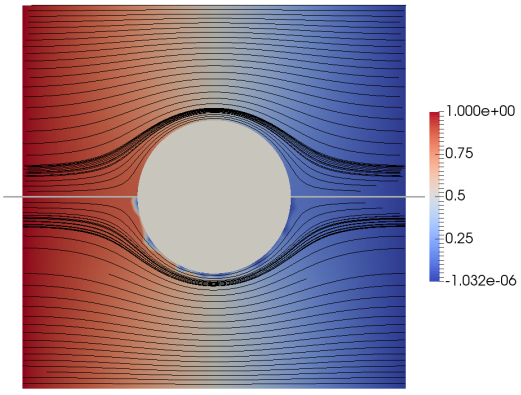

(a) Flux isolines (in black) and pressure. On the top of the grey line is displayed the conformal result and on the bottom the embedded result.

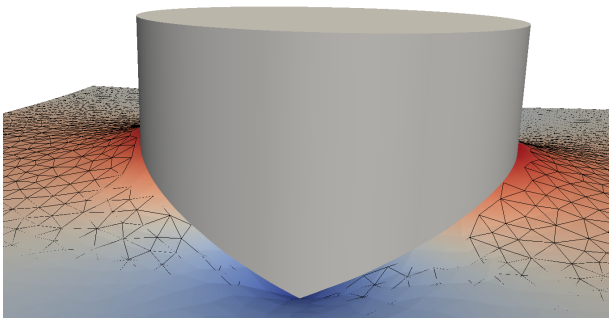

(b) Elevation plots of the flux magnitude close to the cylinder. Conformal simulation : solid contour - Embedded simulation : black wiframe

Figure 17: Circular impermeable obstruction - Comparison between embedded and conformal simulation

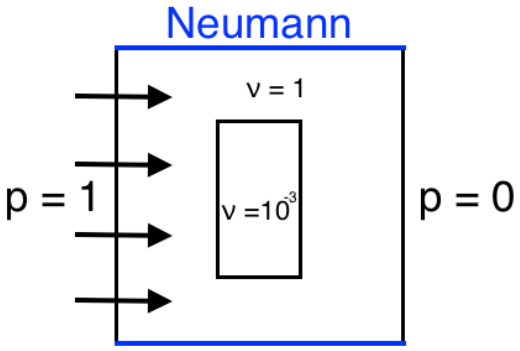

(a) Set up

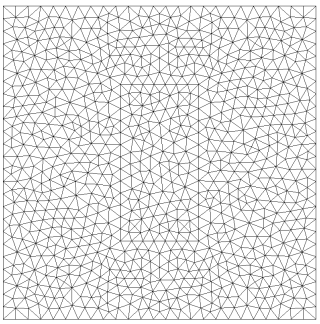

(b) Fitted mesh

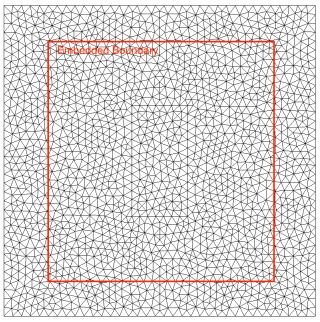

(c) Embedded mesh

Figure 18: Low Permeability obstruction test case

7.4 Flow in a domain with a low permeability obstruction

A square domain $\Omega = [0,1] \times [0,1]$ is divided into two regions. An inner rectangular region of sizes $[\frac{3}{8}, \frac{5}{8}] \times [\frac{1}{4}, \frac{3}{4}]$ with low permeability $\boldsymbol{\Lambda} = 10^{-3}\mathbb{I}$ is surrouded by an area of permeability $\boldsymbol{\Lambda} = \mathbb{I}$. The boundary conditions are a pressure of $p = 1$ and $p = 0$ on respectively left and right sides of the domain and Neumann condition with $\boldsymbol{\beta} \cdot \boldsymbol{n} = 0$ on top and bottom sides (see Figure 18(a)). For embedded simulation, the entire domain is embedded in a bigger square. As this test presents discontinuity in the permeability, the DG scheme has to be used so as to accurately solve the problem. Meshes are presented on Figures 18(b) and 18(c). We propose a comparison of the solution obtained with the conformal and embedded simulation on Figure 19. Once again, one can appreciate the similarities between the two results, which validate once again the discontinuous embedded discretisation.

7.5 A 3D convergence test

Before performing simulation of flow around 3D solid with slip wall boundary conditions (Neumann), we propose to briefly check the convergence rates obtained for such problem in 3D. We embed a sphere of radius $r_{in} = 0.2$ in a bigger sphere of radius $r_{out} = 0.5$. The simulations are performed on 6 levels of refinement, from a mesh of 330 nodes and $1,420$ tetrahedron to a mesh

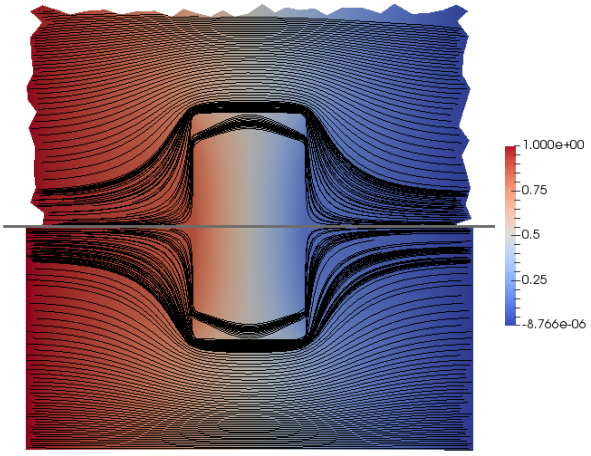

Figure 19: Low permeability obstruction - Comparison of embedded and conformal simulations. Flux isolines on top of pressure contours.

of $7,838,897$ nodes and $46,530,560$ tetrahedrons. The solution is defined as:

$$\begin{cases} \boldsymbol{\beta}(\boldsymbol{x}) = -\dfrac{1}{6}\begin{bmatrix} \cos(x)(\sinh(z)+\sinh(y))+6x \\ \cos(y)\sinh(z)+\sin(x)\cosh(y)+2y \\ \cosh(z)(\sin(y)+\sin(x))-2z \end{bmatrix} \\ p(\boldsymbol{x}) = \dfrac{1}{6}\left(\sinh(z)(\sin(y)+\sin(x))+\sin(x)\sinh(y)+3x^2+y^2-z^2\right) \\ \phi(\boldsymbol{x}) = -1 \\ \boldsymbol{\Lambda} = \mathbb{I} \end{cases} \tag{55}$$

The convergence rates obtained with and without the pressure enrichment are plotted on Figure 20. We can appreciate the similar behavior than for 2D test cases, meaning a second order flux and pressure with the activation of the pressure enrichment that falls back to first order when no specific treatment is done.

7.6 Flow past a complicated three-dimensional object

We propose to simulate the flow around the complicated object named "Monkey Trefoil" already employed in [27], shown in Figure 21. The surface is embedded in a domain of size $[-4,4]\times[-2,2]\times[-4,4]$ and meshed with $9,764,152$ tetrahedra. Dirichlet boundary conditions are applied on $x=\pm 4$ with $p=1$ and $p=0$. Neumann conditions are applied on the other sides of the domain, as well as on the embedded body. Flux isolines and pressure isosurfaces are proposed on Figures 22(a) and 22(b). Those results demonstrate the ability of the proposed approach to solve accurately when complex geometry are involved.

8 Conclusion

We have discussed in this paper an improved version of the shifted boundary method for Darcy equations. By properly exploiting the additional information provided by the mixed form of the

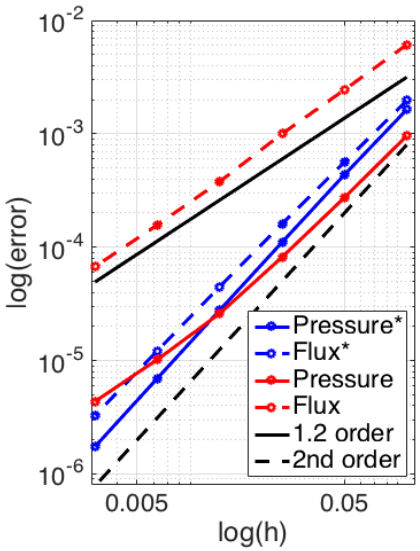

Figure 20: Embedded Neumann 3D simulation - Convergence rates

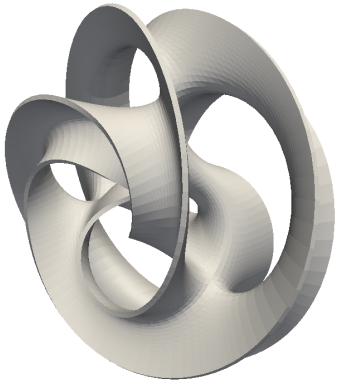

Figure 21: Monkey trefoil shape

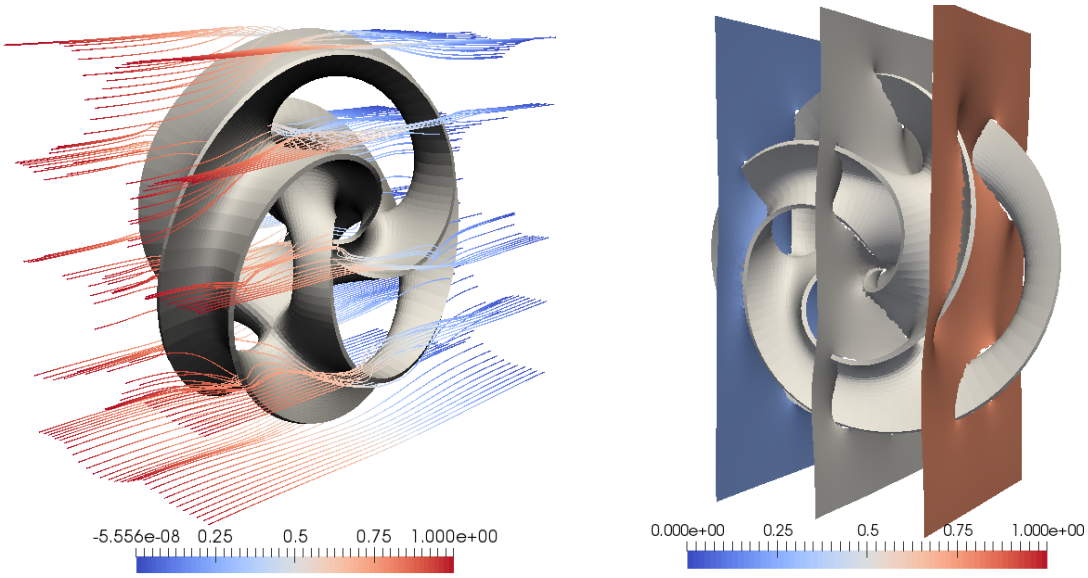

(a) Flux isolines colored by pressure

(b) Pressure isosurface

Figure 22: Monkey trefoil solution

problem to construct and enriched approximation of the pressure, and by enhancing the boundary conditions accordingly, we have shown how to construct an embedded method allowing to obtain second order of accuracy on unstructured grids for both the pressure and the flux, with a third order approximation of the pressure whenever Neumann Boundaries are not embedded. The method has been shown to recover exactly linear and quadratic solutions.

An exhaustive list of test cases has been performed so as to validate the approach and demonstrate the robustness of the schemes, also when strong discontinuities in the permeability exist.

Acknowledgments

This work has partially benefitted from the support of the Associated Team HAMSTER between Duke University and the CARDAMOM INRIA team.

References

References

[1] Frédéric Alauzet. A changing-topology moving mesh technique for large displacements. *Engineering with Computers*, 30(2):175–200, Apr 2014.

[2] Frédéric Alauzet and David Marcum. A closed advancing-layer method with connectivity optimization-based mesh movement for viscous mesh generation. *Engineering with Computers*, 31(3):545–560, Jul 2015.

[3] D. Arnold, F. Brezzi, B. Cockburn, and L. Marini. Unified analysis of discontinuous galerkin methods for elliptic problems. *SIAM Journal on Numerical Analysis*, 39(5):1749–1779, 2002.

[4] Santiago Badia and Ramon Codina. Stabilized continuous and discontinuous galerkin techniques for darcy flow. *Computer Methods in Applied Mechanics and Engineering*, 199(25):1654 – 1667, 2010.

[5] Laure Billon, Youssef Mesri, and Elie Hachem. Anisotropic boundary layer mesh generation for immersed complex geometries. *Engineering with Computers*, 33(2):249–260, Apr 2017.

[6] D. Caraeni and L. Fuchs. Compact third-order multidimensional upwind scheme for navier–stokes simulations. *Theoret Comput Fluid Dynamics*, 15:373–401.

[7] D. K. Clarke, H. A. Hassan, and M. D. Salas. Euler calculations for multielement airfoils using cartesian grids. *AIAA Journal*, 24(3):353–358, 1986.

[8] B. Cockburn, B. Dong, J. Guzmán, M. Restelli, and R. Sacco. A hybridizable discontinuous galerkin method for steady-state convection-diffusion-reaction problems. *SIAM Journal on Scientific Computing*, 31(5):3827–3846, 2009.

[9] Bernardo Cockburn, George E. Karniadakis, and Chi-Wang Shu. *Discontinuous Galerkin Methods: Theory, Computation and Applications*.

[10] Jim Douglas and Todd Dupont. Interior penalty procedures for elliptic and parabolic galerkin methods. In R. Glowinski and J. L. Lions, editors, *Computing Methods in Applied Sciences*, pages 207–216, Berlin, Heidelberg, 1976. Springer Berlin Heidelberg.

[11] Jim Douglas, Mary Fanett Wheeler, Bruce L. Darlow, and Richard P. Kendall. Self-adaptive finite element simulation of miscible displacement in porous media. *Computer Methods in Applied Mechanics and Engineering*, 47(1):131 – 159, 1984. Special Issue on Oil Reservoir Simulation.

[12] A. Ern and J.-L. Guermond. *Theory and practice of finite elements*, volume 159 of *Applied Mathematical Sciences*. Springer, 2004.

[13] Boyce E. Griffith, Richard D. Hornung, David M. McQueen, and Charles S. Peskin. An adaptive, formally second order accurate version of the immersed boundary method. *Journal of Computational Physics*, 223(1):10 – 49, 2007.

[14] Boyce E. Griffith and Charles S. Peskin. On the order of accuracy of the immersed boundary method: Higher order convergence rates for sufficiently smooth problems. *Journal of Computational Physics*, 208(1):75 – 105, 2005.

[15] E. Hachem, S. Feghali, R. Codina, and T. Coupez. Immersed stress method for fluid–structure interaction using anisotropic mesh adaptation. *International Journal for Numerical Methods in Engineering*, 94(9):805–825, 2013.

[16] Anita Hansbo and Peter Hansbo. An unfitted finite element method, based on nitsche's method, for elliptic interface problems. *Computer Methods in Applied Mechanics and Engineering*, 191(47):5537 – 5552, 2002.

[17] H. Huang and G. Scovazzi. A high-order, fully coupled, upwind, compact discontinuous galerkin method for modeling of viscous fingering in compressible porous media. *Computer Methods in Applied Mechanics and Engineering*, 263:169 – 187, 2013.

[18] Thomas J.R. Hughes, Arif Masud, and Jing Wan. A stabilized mixed discontinuous galerkin method for darcy flow. *Computer Methods in Applied Mechanics and Engineering*, 195(25):3347 – 3381, 2006. Discontinuous Galerkin Methods.

[19] Thomas J.R. Hughes, Guglielmo Scovazzi, Pavel B. Bochev, and Annalisa Buffa. A multiscale discontinuous galerkin method with the computational structure of a continuous galerkin method. *Computer Methods in Applied Mechanics and Engineering*, 195(19):2761 – 2787, 2006.

[20] A.A. Johnson and T.E. Tezduyar. Mesh update strategies in parallel finite element computations of flow problems with moving boundaries and interfaces. *Computer Methods in Applied Mechanics and Engineering*, 119(1):73 – 94, 1994.

[21] A.A. Johnson and T.E. Tezduyar. Simulation of multiple spheres falling in a liquid-filled tube. *Computer Methods in Applied Mechanics and Engineering*, 134(3):351 – 373, 1996.

[22] Rooh. A. Khurram and Arif Masud. A multiscale/stabilized formulation of the incompressible navier–stokes equations for moving boundary flows and fluid–structure interaction. *Computational Mechanics*, 38(4):403–416, Sep 2006.

[23] M.P. Kirkpatrick, S.W. Armfield, and J.H. Kent. A representation of curved boundaries for the solution of the navier–stokes equations on a staggered three-dimensional cartesian grid. *Journal of Computational Physics*, 184(1):1 – 36, 2003.

[24] S. Lee, Y. Lee, and M. Wheeler. A locally conservative enriched galerkin approximation and efficient solver for elliptic and parabolic problems. *SIAM Journal on Scientific Computing*, 38(3):A1404–A1429, 2016.

[25] Randall J. LeVeque and Zhilin Li. Immersed interface methods for stokes flow with elastic boundaries or surface tension. *SIAM Journal on Scientific Computing*, 18(3):709–735, 1997.

[26] Mark N. Linnick and Hermann F. Fasel. A high-order immersed interface method for simulating unsteady incompressible flows on irregular domains. *Journal of Computational Physics*, 204(1):157 – 192, 2005.

[27] A. Main and G. Scovazzi. The shifted boundary method for embedded domain computations. part i: Poisson and stokes problems. *Journal of Computational Physics*, 2017.

[28] A. Main and G. Scovazzi. The shifted boundary method for embedded domain computations. part ii: Linear advection–diffusion and incompressible navier–stokes equations. *Journal of Computational Physics*, 2018.

[29] Arif Masud and Thomas J.R. Hughes. A stabilized mixed finite element method for darcy flow. *Computer Methods in Applied Mechanics and Engineering*, 191(39):4341 – 4370, 2002.

[30] Alireza Mazaheri and Hiroaki Nishikawa. Improved second-order hyperbolic residual-distribution scheme and its extension to third-order on arbitrary triangular grids. *Journal of Computational Physics*, 300:455 – 491, 2015.

[31] Alireza Mazaheri and Hiroaki Nishikawa. Efficient high-order discontinuous galerkin schemes with first-order hyperbolic advection–diffusion system approach. *Journal of Computational Physics*, 321:729 – 754, 2016.

[32] Alireza Mazaheri, Mario Ricchiuto, and Hiroaki Nishikawa. A first-order hyperbolic system approach for dispersion. *Journal of Computational Physics*, 321:593 – 605, 2016.

[33] Rajat Mittal and Gianluca Iaccarino. Immersed boundary methods. *Annual Review of Fluid Mechanics*, 37(1):239–261, 2005.

[34] Hiroaki Nishikawa. Robust and accurate viscous discretization via upwind scheme – i: Basic principle. *Computers & Fluids*, 49(1):62 – 86, 2011.

[35] Hiroaki Nishikawa. On hyperbolic method for diffusion with discontinuous coefficients. *Journal of Computational Physics*, 367:102 – 108, 2018.

[36] J. A. Nitsche. Uber ein Variationsprinzip zur Losung Dirichlet-Problemen bei Verwendung von Teilraumen, die keinen Randbedingungen unteworfen sind. *Abh. Math. Sem. Univ., Hamburg*, 36:9–15, 1971.

[37] L. Nouveau, H. Beaugendre, C. Dobrzynski, R. Abgrall, and M. Ricchiuto. An adaptive, residual based, splitting approach for the penalized navier stokes equations. *Computer Methods in Applied Mechanics and Engineering*, 303:208 – 230, 2016.

[38] Charles S Peskin. Flow patterns around heart valves: A numerical method. *Journal of Computational Physics*, 10(2):252 – 271, 1972.

[39] W.H. Reed and T.R. Hill. Triangular mesh methods for the neutron transport equation. 10 1973.

[40] G. Scovazzi, A. Gerstenberger, and S.S. Collis. A discontinuous galerkin method for gravity-driven viscous fingering instabilities in porous media. *Journal of Computational Physics*, 233:373 – 399, 2013.

[41] T. Song, A. Main, G. Scovazzi, and M. Ricchiuto. The shifted boundary method for hyperbolic systems: Embedded domain computations of linear waves and shallow water flows. *Journal of Computational Physics*, 369:45 – 79, 2018.

[42] Fotis Sotiropoulos and Xiaolei Yang. Immersed boundary methods for simulating fluid–structure interaction. *Progress in Aerospace Sciences*, 65:1 – 21, 2014.

[43] H. S. Udaykumar, W. Shyy, and M. M. Rao. Elafint: A mixed eulerian–lagrangian method for fluid flows with complex and moving boundaries. *International Journal for Numerical Methods in Fluids*, 22(8):691–712, 1996.

[44] Guoyin Wang, Guglielmo Scovazzi, Léo Nouveau, Christopher E. Kees, Simone Rossi, Oriol Colomés, and Alex Main. Dual-scale galerkin methods for darcy flow. *Journal of Computational Physics*, 354:111 – 134, 2018.

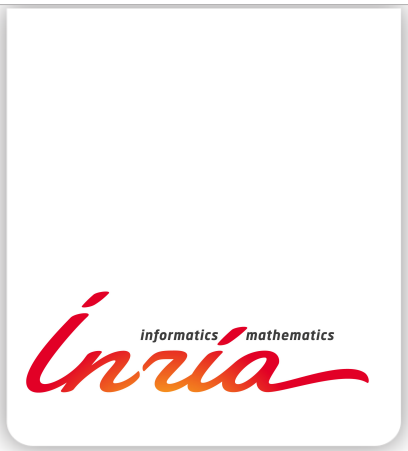

RESEARCH CENTRE
BORDEAUX – SUD-OUEST

200, Avenue de la Vieille Tour
33405 Talence Cedex

Publisher
Inria
Domaine de Voluceau - Rocquencourt
BP 105 - 78153 Le Chesnay Cedex
inria.fr

ISSN 0249-6399